JACS
JOURNAL OF THE AMERICAN CHEMICAL SOCIETY
Article
Cite This: J. Am. Chem. Soc. 2019, 141, 4597−4612
pubs.acs.org/JACS

Excimer Disaggregation Enhanced Emission: A Fluorescence "Turn-On" Approach to Oxoanion Recognition

Jian Yang,[†] Chao-Chen Dong,[†,‡] Xu-Lang Chen,[†] Xin Sun,[†] Jin-Yan Wei,[‡] Jun-Feng Xiang,[§] Jonathan L. Sessler,[∥,⊥] and Han-Yuan Gong[†]

[†]College of Chemistry, Beijing Normal University, Xinjiekouwaidajie 19, Beijing 100875, P. R. China
[‡]Department of Chemistry, Renmin University of China, Beijing 100872, P. R. China
[§]Institute of Chemistry, Chinese Academy of Sciences, Zhongguancunbeiyijie 2, Beijing 100190, P. R. China
[∥]Center for Supramolecular Chemistry and Catalysis, Shanghai University, Shanghai 200444, P. R. China
[⊥]Department of Chemistry, The University of Texas at Austin, 105 East 24th Street, Stop A5300, Austin, Texas 78712-1224, United States

* Supporting Information

ABSTRACT: A new approach to anion sensing that involves excimer disaggregation induced emission (EDIE) is reported. It involves the anion-mediated disaggregation of the excimer formed from a cationic macrocycle. This leads to an increase in the observed fluorescence intensity. The macrocycle in question, cyclo[1]N²,N⁶-dimethyl-N²,N⁶-bis(6-(1H-imidazolium-1-yl)pyridin-2-yl)pyridine-2,6-diamine[1]1,4-dimethylbenzene (1^{2+}; prepared as its PF_6^- salt), is obtained in ca. 70% yield via a simple cyclization. X-ray diffraction analyses of single crystals revealed that, as prepared, this macrocycle exists in a supramolecular polymeric form in the solid state. Macrocycle 1^{2+} is weakly fluorescent in acetonitrile. The emission intensity is concentration dependent, with the maximum intensity being observed at ca. 0.020 mM. This finding is ascribed to formation of an excimer, followed possibly by higher order aggregates as the concentration of 1^{2+} is increased. Addition of tetrabutylammonium pyrophosphate ($HP_2O_7^{3-}$) to 1^{2+} (0.020 mM in acetonitrile) produces a ca. 200-fold enhancement in the emission intensity (λ_{ex} = 334 nm; λ_{em} = 390−650 nm). These findings are rationalized in terms of the $HP_2O_7^{3-}$ serving to break up essentially non-fluorescent excited-state dimers of 1^{2+} through formation of a highly fluorescent anion-bound monomeric complex, $1^{2+}\cdot HP_2O_7^{3-}$. A turn-on in the fluorescence intensity is also seen for $H_2PO_4^-$ and, to a lesser extent, HCO_3^-. Little (HSO_4^-, NO_3^-) or essentially no (N_3^-, SCN^-, F^-, Cl^-, Br^- and I^-) response is seen for other anions. Solid-state structural analysis of single crystals obtained after treating 1^{2+} with $HP_2O_7^{3-}$ in the presence of water revealed a salt form wherein a $H_2P_2O_7^{2-}$ anion sits above the cone-like macrocycle.

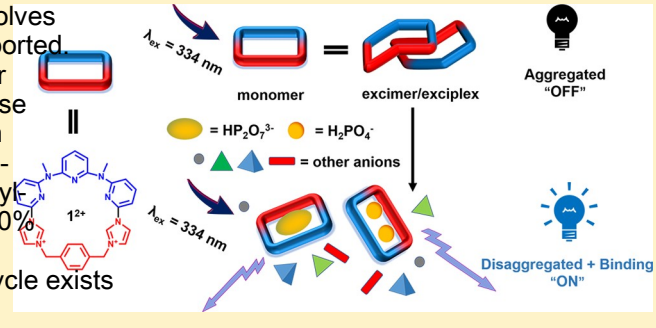

INTRODUCTION

Considerable effort has been dedicated to the design and synthesis of receptors for the recognition and sensing of oxoanion species.[1] Particularly important oxoanions include pyrophosphate ($HP_2O_7^{3-}$), hydrophosphate ($H_2PO_4^-$), bicarbonate (HCO_3^-), and hydrosulfate (HSO_4^-). These species play important roles in living organisms and are widely distributed in the environment.[2] Thus, there is considerable interest in the development of simple systems that will allow for the detection of these and related anionic species.[3] A number of elegant sensors for $HP_2O_7^{3-}$,[4] $H_2PO_4^-$,[5] HCO_3^-,[6] and HSO_4^-[7] have been reported in recent years. Many of these have relied on signal transduction mechanisms, wherein a binding event is translated into a change in an optical or electrochemical output.[8] Other mechanisms that have been exploited in the context of developing so-called "turn-on" fluorescent sensors include photoinduced electron transfer (PET),[9] excimer/exciplex,[10] fluorescence resonance energy transfer (FRET),[11] intramolecular charge transfer (ICT),[12] excited-state intra-/intermolecular proton transfer (ESIPT),[13] and aggregation-induced emission (AIE).[14] However, the development of new mechanisms for sensing remains important. We believe it could contribute to the generalized problem of anion sensing beyond the specific problem of oxoanion recognition.[15] Here, we report what is to the best of our knowledge a new approach to anion sensing that involves excimer disaggregation induced emission (EDIE). Briefly, disaggregation mediated by anion binding in acetonitrile, converts a weakly fluorescent species into one with considerably greater emission intensity. The net result is an easy-to-discern increase ("turn-on") in the overall fluorescence

Received: August 21, 2018
Published: February 24, 2019

DOI: 10.1021/jacs.8b09021
J. Am. Chem. Soc. 2019, 141, 4597−4612

signature. The present approach, summarized graphically in Scheme 1, could provide a useful complement to strategies

Scheme 1. Anion Recognition Modes and Schematic View of the Excimer Disaggregation Induced Emission (EDIE) Sensing Mechanism Proposed for $1^{2+}\cdot 2PF_6^-$

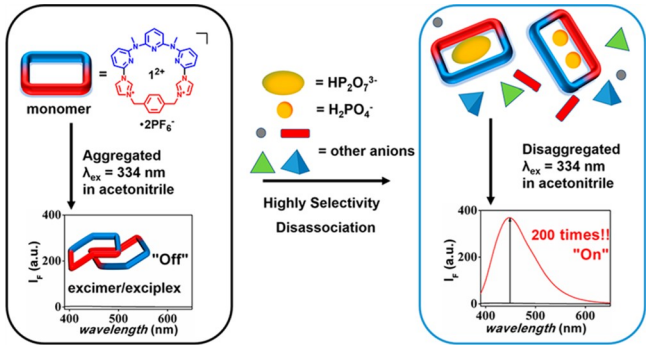

involving the breakup of ground-state aggregates.[16] The importance of the latter mechanism has recently been underscored in the context of sugar recognition.[17] However, with the exception of early work from our group,[18] it has rarely been exploited for anion sensing.

The dimeric excimer used in the present study is produced by dissolving the bis-PF_6^- salt of a new pyridine imidazolium macrocycle, namely cyclo[1]N^2,N^6-dimethyl-N^2,N^6-bis(6-(1H-imidazolium-1-yl)pyridin-2-yl)pyridine-2,6-diamine[1]1,4-dimethylbenzene (1^{2+}), in acetonitrile at concentrations >0.010 mM and subjecting it to photo-illumination (λ_{ex} = 334 or 415 nm). As discussed below, addition of oxoanionic species leads to a turn-on in the fluorescence of 1^{2+}, with the $HP_2O_7^{3-}$ and $H_2PO_4^-$ anions (both as their tetrabutylammonium (TBA$^+$) salts) proving particularly effective. Little interference from other anions is seen. These results are rationalized in terms of competitive binding (self-association vs anion recognition) and are supported by solid-state structural analyses.

RESULTS AND DISCUSSION

Synthesis and Structural Analysis of 1^{2+}. Macrocycle 1^{2+} was synthesized as shown in Scheme 2. Following a procedure reported in the literature,[19,20] N^2,N^6-bis(6-bromopyridin-2-yl)-N^2,N^6-dimethylpyridine-2,6-diamine (2) was obtained in a total yield of 72%. An Ullmann coupling was used to generate N^2,N^6-bis(6-1H-imidazol)-N^2,N^6-dimethylpyridine-2,6-diamine (3) in 94% yield.[21] Reaction of 3 with 1,4-bis(bromomethyl)benzene gave $1^{2+}\cdot 2Br^-$. Following anion exchange via treatment with NH_4PF_6 in water, the target system 1^{2+} (as its bis-PF_6^- salt) was obtained in up to 70% yield.

Scheme 2. Synthesis of Macrocycle $1^{2+}\cdot 2PF_6^-$

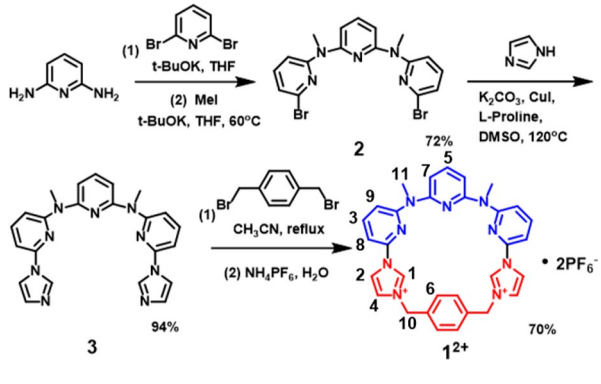

Macrocycle 1^{2+} is comprised of two "halves", both of which were expected to impart anion recognition capability. The top "half" consists of an N^2,N^6-dimethyl-N^2,N^6-bispyridin-2-yl)-pyridine-2,6-diamine moiety (blue part of 1^{2+} in Scheme 2), a subunit that has previously been demonstrated to be an effective intermolecular hydrogen bond acceptor.[19−21] A 1,4-bis((1H-imidazolium-1-yl)methyl)benzene (red part of 1^{2+} shown in Scheme 2) makes up the lower half. This latter fragment contains both cationic imidazolium and neutral benzene C−H potential hydrogen bond donors. Macrocycle 1^{2+} was thus expected to function as an anion receptor under appropriate conditions. The two halves of 1^{2+} are bridged by single bonds. It was anticipated that the resulting flexibility would allow for conformational motion and permit the overall structure to undergo the adjustments needed to optimize guest binding.

Evidence for the conformational flexibility of macrocycle 1^{2+} came from ^{1}H NMR and two-dimensional nuclear Overhauser effect spectroscopy (NOESY) studies carried out at 298 K in CD_3CN-d_3 (cf. Supporting Information (SI)). Only one set of high-resolution signals is seen in the ^{1}H NMR spectrum of 1^{2+}. In the NOESY spectrum, corresponding signals between H(1,4) and H(6), as well as H(1,2) and H(8), are observed. We thus propose that 1^{2+} is subject to dynamic motion in solution, at least on the NMR time scale.

Further support for the conformational flexibility of 1^{2+} came from single-crystal X-ray diffraction analyses. Specifically, two different sets of diffraction-grade single crystals of $1^{2+}\cdot 2PF_6^-$ were obtained, depending on the specific crystallization conditions employed (cf. SI). Different symmetries, C_s vs C_1, were seen in the resulting structures, which proved to be those of $1^{2+}\cdot 2PF_6^-\cdot 2CH_3CN\cdot 0.25H_2O$ and $1^{2+}\cdot 2PF_6^-\cdot$dioxane, respectively (Figure 1). Two different bowl-like cavities were also seen in the two structures. However, in both cases, the pyridine nitrogen atoms and the two imidazolium C−H bonds on the (6-(1H-imidazolium-1-yl)pyridin-2-yl) moieties point to the

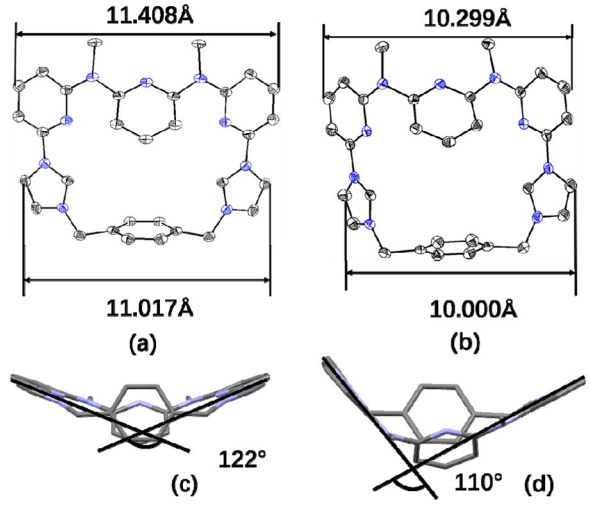

Figure 1. Top (ellipsoid representation) and side (stick representation) views of 1^{2+} seen in the single-crystal structures of $1^{2+}\cdot 2PF_6^-\cdot 2CH_3CN\cdot 0.25H_2O$ and $1^{2+}\cdot 2PF_6^-\cdot$dioxane shown in (a), (c) and (b), (d), respectively.

DOI: 10.1021/jacs.8b09021
J. Am. Chem. Soc. 2019, 141, 4597−4612

bottom of the bowl (cf. SI). The aromatic rings on the opposing N^2,N^6-dimethylpyridine-2,6-diamine and 1,4-dimethylbenzene fragments are also oriented toward the bottom of the bowl (cf. SI). The net result is a set of structural features, including the orientation of several putative C−H hydrogen bond donors, that were expected to make 1^{2+} effective as an anion receptor.

Pyrophosphate Anion Binding Properties of 1^{2+}. Based on considerations of size and geometry, $HP_2O_7^{3-}$ (TBA^+ salt) was chosen as a first oxoanionic guest with which to test the anion binding properties of 1^{2+}. UV−vis and ^{1}H NMR spectroscopic methods, as well as isothermal titration calorimetry (ITC), were then used to probe the interactions in acetonitrile (or acetonitrile-d_3). A Job plot analysis based on the UV−vis spectroscopic changes observed as a function of concentration ([H] + [G] = 0.050 mM) revealed a peak value at a mole fraction of 0.5. Clean isosbestic behavior was also seen. On this basis, we propose that a 1:1 (host/guest) stoichiometry best describes the binding interaction between 1^{2+} and $HP_2O_7^{3-}$ (cf. SI).

Further support for the proposal that receptor 1^{2+} is able to interact with $HP_2O_7^{3-}$ came from a mass spectrometric study. In particular, a peak with an m/z of 702.1749 was observed under conditions of electrospray ionization high-resolution mass spectrometry (ESI-HRMS) from an initial aqueous solution containing 1^{2+} and $HP_2O_7^{3-}$ (vide infra). Such a finding is in accord with what would be expected for a 1:1 complex formed between 1^{2+} and $HP_2O_7^{3-}$ (calculated for $C_{31}H_{30}N_9O_7P_2$; $[1^{2+}\cdot HP_2O_7^{3-}]^-$ = 702.1749]) in the gas phase (cf. SI). Diagnostic shifts in the ^{1}H NMR spectrum were also seen when $HP_2O_7^{3-}$ was added into an acetonitrile-d_3 solution of $1^{2+}\cdot 2PF_6^-$ (cf. SI).

The charged nature of 1^{2+} led us to consider that, in analogy to what proved true for protonated sapphyrin[18] and europium-adjusted carbon dots[22], this flexible macrocyclic receptor might prove effective as a disaggregation-based sensor for the four test oxoanions for which spectroscopic evidence of binding was obtained (vide infra). As a predicate to these studies, we sought to explore whether 1^{2+} was appreciably aggregated in acetonitrile solution. Initial tests involved Beer−Lambert plots. Over a wide range of concentrations, no appreciable differences in the extinction coefficients were seen (Figure 2 and SI, Figures S10 and S11). Likewise, no charge-transfer (CT) band corresponding to ground-state aggregation was seen at higher concentrations. On this basis, we conclude that the ground-state form of 1^{2+} is not appreciably aggregated. It was thus not expected to function as a fluorescent turn-on sensor based on the simple breakup of ground-state aggregates.

When irradiated at a λ_{ex} = 334 nm, 0.020 mM solutions of $1^{2+}\cdot 2PF_6^-$ in CH_3CN proved essentially non-emissive. However, the fluorescence emission intensity was found to increase monotonically as a function of increasing $HP_2O_7^{3-}$ concentration (TBA^+ salt; from 0 to 0.021 mM) at 298 K (cf. Figure 3). An effort was then made to quantify the presumed interactions. Toward this end, the integrated fluorescence intensity between 395 and 650 nm was plotted as a function of $HP_2O_7^{3-}$ concentration with $[1^{2+}\cdot 2PF_6^-]$ held constant at 0.020 mM (Figure 3 inset). Importantly, the fluorescent features of any given set of solutions produced by adding $HP_2O_7^{3-}$ to acetonitrile solutions of $1^{2+}\cdot 2PF_6^-$ proved highly reproducible. Moreover, no appreciable changes in the emission values were observed even after subjecting the solutions to 30 independent analyses

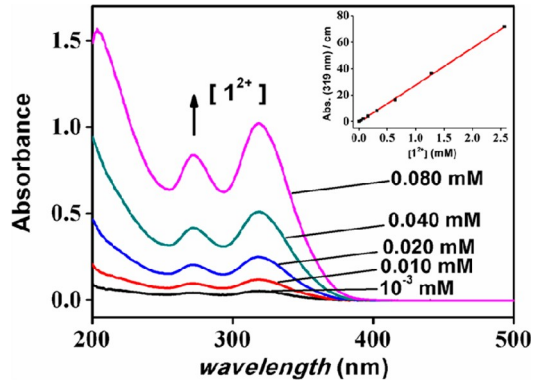

Figure 2. Concentration-dependent UV−vis spectra of $1^{2+}\cdot 2PF_6^-$ recorded at 1.00 × 10^{-3} mM (black line), 0.010 mM (red line), 0.020 mM (blue line), 0.040 mM (green line), and 0.080 mM (pink line) in acetonitrile. Inset shows the normalized spectral intensity at 319 nm (▪) recorded over the 1.00 × 10^{-3} mM and 2.56 mM) concentration range. The red line corresponds to an associated linear fit (created via the linear expression $Abs_{(319\ nm)}$ = (13.9 ± 0.2) × $[1^{2+}]$ with adjusted R^2 = 0.997) assuming Beer−Lambert behavior.

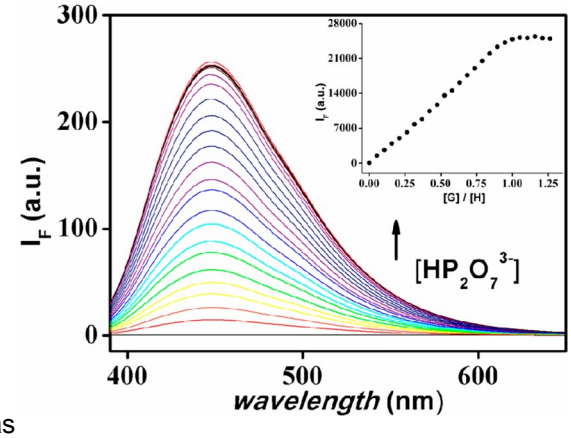

Figure 3. Fluorescent emission spectra of a solution containing $1^{2+}\cdot 2PF_6^-$ (0.020 mM) in CH_3CN as a function of increasing $HP_2O_7^{3-}$ concentration (TBA^+ salt; from 0 to 0.026 mM) at 298 K. λ_{ex} = 334 nm. Voltage = 400 V, entrance slit width = 5 nm, exit slit width = 10 nm. Inset shows the corresponding change in the integrated fluorescence intensity between 390 and 650 nm (▪).

(i.e., repeated scans under conditions of fluorescence analysis; cf. Figure S35).

Since $1^{2+}\cdot 2PF_6^-$ on its own displays little in the way of fluorescence, at least as a 0.020 mM solution in CH_3CN, and the pyrophosphate salt itself is likewise non-emissive, the above quantitative analysis leaves unanswered the specific origin of the increase in fluorescence emission intensity observed as $HP_2O_7^{3-}$ is added to 0.020 mM solutions of $1^{2+}\cdot 2PF_6^-$ in CH_3CN. As a first step in an effort to understand the underlying determinants, the packing diagrams of the structures of $[1^{2+}\cdot 2PF_6^-\cdot 2CH_3CN\cdot 0.25H_2O]$ and $[1^{2+}\cdot 2PF_6^-\cdot$ dioxane] discussed above were analyzed. This analysis revealed interactions between neighboring macrocycles (Figure 4a−d). Single crystals of the pyrophosphate salt were then grown. The resulting structure $[1^{2+}\cdot H_2P_2O_7^{2-}\cdot 4H_2O]$ revealed a sitting-top anion complex and reduced interactions between the individual macrocycles (Figure 4e and SI). Although not a proof, such a finding lends support to the suggestion that break up of an excimer contributes to the pyrophosphate anion-

DOI: 10.1021/jacs.8b09021
J. Am. Chem. Soc. 2019, 141, 4597−4612

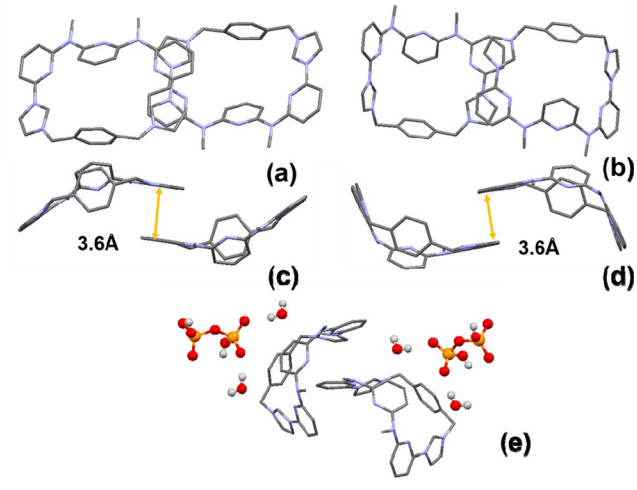

Figure 4. Single-crystal X-ray diffraction structures of $[1^{2+}\cdot 2PF_6^-\cdot 2CH_3CN\cdot 0.25H_2O]$ shown in top (a) and front (c) views, $[1^{2+}\cdot 2PF_6^-\cdot$ dioxane] shown in top (b) and front (d) views, and (e) $[1^{2+}\cdot H_2P_2O_7^{2-}\cdot 4H_2O]$. Close contacts between individual units neighboring macrocycles 1^{2+} units (shown with orange double headed arrows) are observed in the first two of these three structures.

induced increase in fluorescence intensity seen in dilute acetonitrile solution.

Monomer−Dimeric Excimer Equilibrium Model. The fluorescence emission features of $1^{2+}\cdot 2PF_6^-$ were then analyzed in detail over a wide range of relatively low concentrations, namely from 2.50×10^{-4} mM to 0.100 mM in acetonitrile. At the lowest of these concentrations a non-aggregated form was expected to dominate. Thus, an excitation wavelength (λ_{ex}) of 334 nm, corresponding to the maximum emission intensity at 415 nm of the monomeric form, was used. For a well-behaved system, the intensity was expected to increase linearly with concentration. This was not seen (Figure 5). In fact, the maximum fluorescence intensity for the monomer (integrated over the 390−650 nm spectral region) was seen when the concentration of $1^{2+}\cdot 2PF_6^-$ was 0.020 mM. The fluorescence intensity then decreases as the concentration of $1^{2+}\cdot 2PF_6^-$ is raised. Meanwhile, a new shoulder appears at around 500 nm when the concentration of $1^{2+}\cdot 2PF_6^-$ is higher than 0.030 mM, a finding consistent with the formation of an excimer (cf. SI).

The above findings lead us to suggest that individual units of 1^{2+} dimerize to form excimers, which might possibly self-associate further to form higher order aggregates. Normalization of the data across the full concentration range reveals that it is the monomeric form that is most fluorescent (highest quantum yield) on a per mole basis. Therefore, it was tentatively concluded that addition of pyrophosphate serves to break up the aggregated forms of 1^{2+}, particularly the dimeric excimer that is expected to dominate over most of the 2.50×10^{-4} mM to 0.100 mM concentration range associated with this study. Efforts were thus made to study this proposed phenomenon in detail.

More direct evidence for excimer formation in the case of $1^{2+}\cdot 2PF_6^-$ came from experiments involving excitation at 334 and 415 nm, respectively. Excitation at 334 nm led to a monomer-like emission at 415 nm as well as a weak excimer emission at around 500 nm when the concentration of $1^{2+}\cdot 2PF_6^-$ is high (larger than 0.030 mM). In contrast, excitation at 415 nm gave rise to emission at 480 nm over a wide range of concentrations (Figure 6). When the concentration of $1^{2+}\cdot 2PF_6^-$ is higher than 0.32 mM, a linear relationship between the fluorescence intensity at 480 nm and the concentration of $1^{2+}\cdot 2PF_6^-$ is observed.

Additional support for the proposed excimer formation in the case of 1^{2+} came from excitation spectral studies. When scans were carried out with monitoring at λ_{em} = 415 and 480 nm (cf. Figures S14 and S15), the excitation profile proved similar to that of the UV−vis spectrum of $1^{2+}\cdot 2PF_6^-$, provided the concentration of $1^{2+}\cdot 2PF_6^-$ was kept lower than 0.100 mM. Increasing the concentration of $1^{2+}\cdot 2PF_6^-$ from 0.001 to 2.56 mM led to a decrease in the intensity of the peaks at 270 and 300 nm seen in the excitation scans recorded at $[1^{2+}\cdot 2PF_6^-]$ < 0.100 mM. These latter peaks were essentially absent at the highest concentrations. Meanwhile, the longest wavelength feature at 372 nm was seen to undergo a red shift to 390 nm as the concentration increased, with a commensurate increase in spectral intensity being observed (cf. Figures S14 and S15). Taken in concert, these findings are consistent with a dimeric excimer being stabilized at relatively high concentrations. This species displays a maximal fluorescence intensity at 480 nm

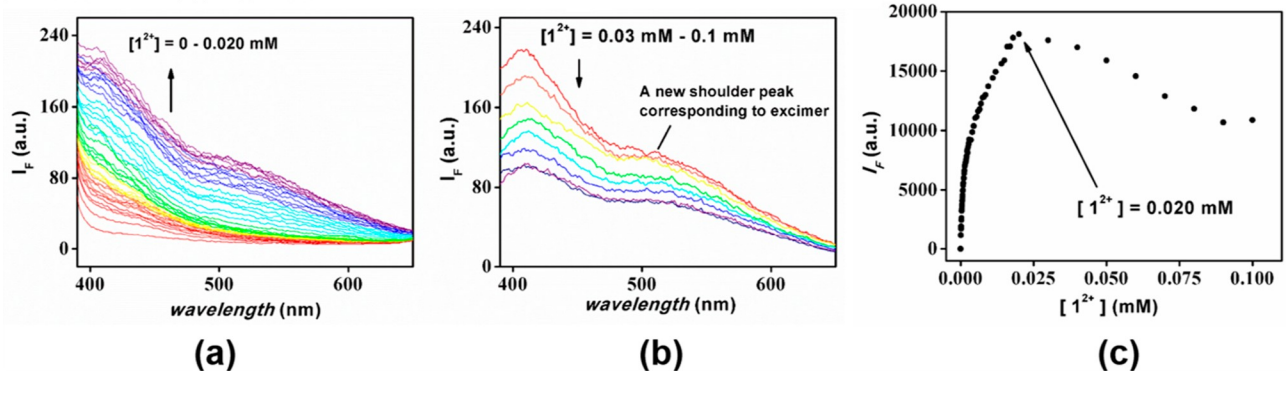

Figure 5. Selected concentration-dependent fluorescent emission spectra for $1^{2+}\cdot 2PF_6^-$ are shown in (a) and (b). Shown in (c) is a plot of the corresponding change in the value of the integrated emission intensity between 390 and 650 nm as the concentration was varied from 2.50×10^{-4} mM to 0.100 mM in acetonitrile (•). As discussed in the text, this emission intensity is ascribed to the monomeric form. (λ_{ex} = 334 nm, voltage = 900 V, entrance slit width = 5 nm, exit slit width = 10 nm. Note: The fluorescence spectra of concentrations of 0.001, 0.010, and 0.020 mM were independently remeasured (scanned) 30 times. No appreciable differences were seen upon repeat scans. This leads us to suggest that the system is stable under the study conditions.

DOI: 10.1021/jacs.8b09021
J. Am. Chem. Soc. 2019, 141, 4597−4612

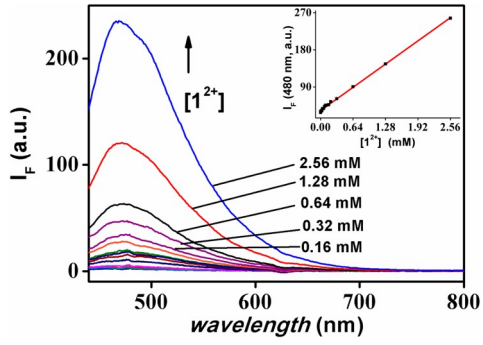

Figure 6. Concentration-dependent fluorescence emission spectra of $1^{2+}\cdot 2PF_6^-$ in acetonitrile recorded from 2.00 × 10^{-4} mM to 2.56 mM using λ_{ex} = 415 nm. Voltage = 700 V, entrance slit width = 5 nm, exit slit width = 10 nm. Inset shows the corresponding change in the emission intensity value at 480 nm as a function of concentration. The red line was created using the linear expression $I_{F(480\ nm)}$ = (88.0 ± 1.0) × [1^{2+}] + (32.7 ± 0.7), giving an adjusted R^2 = 0.998.

when photoexcitation is affected at 415 nm (cf. Table 1). Importantly, it is substantially less emissive than the monomeric form as noted above.

Table 1. Excitation Wavelengths (λ_{ex}) and Maximum Fluorescence Intensity Wavelengths of 1^{2+} (λ_{em})

species	λ_{ex} (nm)	λ_{em} (nm)
1^{2+}	334	415
$(1^{2+})_2$	334	~500[a]
	415	480
$1^{2+}\cdot HP_2O_7^{3-}$	334	445

[a]A shoulder located at around 500 nm is observed when the concentration of $1^{2+}\cdot 2PF_6^-$ is larger than 0.030 mM.

Quantitative analyses of the concentration-dependent fluorescence spectral features were then carried out in an effort to determine the contributions of the monomer and excimer of $1^{2+}\cdot 2PF_6^-$, respectively, to the overall emission intensity.

To test whether a simple monomer−dimeric excimer model could be used to describe the experimental observations seen in acetonitrile at relatively low concentrations ([$1^{2+}\cdot 2PF_6^-$] = $[u]_0$ = 2.5 × 10^{-4} mM to 0.020 mM), the following elementary reactions were considered in the context of a global kinetic analysis:

$$u + h\nu_1 \xrightarrow{j_1} u^* \quad \text{(i)}$$

$$u^* \xrightarrow{j_2} u + h\nu_2 \quad \text{(ii)}$$

$$u^* + M \xrightarrow{k_1} u + M \quad \text{(iii)}$$

$$u^* + u \xrightarrow{k_2} u_2^* \quad \text{(iv)}$$

$$u_2^* + M \xrightarrow{k_3} u + M \quad \text{(v)}$$

where u is 1^{2+} in the ground state; u* is 1^{2+} in the excited state under irritation (λ_{ex} = 334 nm); u_2^* is the non-fluorescent dimeric excimer of 1^{2+}; M is media which induced the relaxation of the species in the excited state; $h\nu_1$ is the light intensity at the excitation wavelength of 334 nm interacting with 1^{2+} and reflects the absorbance (A) value at that wavelength; $h\nu_2$ is the integrated emission intensity over the 390−650 nm spectral region. Parameters j_1, j_2, k_1, k_2, and k_3 are rate constants of the individual (but inter-related) elementary reactions. In this model, the effects of media (including solvent, acetonitrile, and counteranion, PF_6^-) are ignored, as are the potential effects of higher order aggregates. Thus, it is assumed that the sole aggregation product of 1^{2+} (u) is the non-fluorescent dimeric excimer, u_2^*.

At the limit where the total concentration of 1^{2+} ($[u]_0$) is zero ($[u]_0 \to 0$), elementary reactions involving u_2^* (namely elementary reactions iv and v) may be ignored. Thus, the theoretical quantum yield of the emitting monomeric species 1^{2+} (i.e., $\phi_{u(monomer)}$) can be calculated using elementary reactions i−iii. Accordingly, only monomeric species were considered in the following equilibrium expression (eq 1):

$$[u]_0 = [u]_{monomer} = [u] + [u^*] \quad (1)$$

Here, $[u]_0$ is the total concentration of 1^{2+}; $[u]_{monomer}$ is the concentration of the monomeric forms of 1^{2+} and is the sum of 1^{2+} in the ground state (i.e., [u]) and in the excited state (i.e., [u*]).

With $[u]_0 \to 0$, the observed emission intensity (F_{obs} = $F_{[u]_0\to 0}$) can be expressed as eq 2:

$$\frac{F_{[u]_0\to 0}}{A_{[u]_0\to 0}\phi_{u(monomer)}} = \frac{F_s}{A_s\phi_s} \quad (2)$$

In eq 2, $A_{[u]_0\to 0}$ is the absorbance of 1^{2+} at 334 nm, a value that obeys the Beer−Lambert law (vide supra and eq 3). As noted above, F_s = 4.87 × 10^6, A_s = 0.0104, and ϕ_s = 0.556 are, respectively, the detected emission intensity between 390 and 650 nm, the absorbance value at 334 nm, and the quantum yield of a reference standard (i.e., a solution of quinine bisulfate in 0.1 N sulfuric acid[29]).

$$A_{[u]} = \varepsilon_u[u]_0 l \quad (3)$$

Combining eqs 2 and 3 gives the equilibrium expression governing $\phi_{u(monomer)}$ as eq 4:

$$\phi_{u(monomer)} = \frac{F_{[u]\to 0}}{\varepsilon_u[u]_0 l}\frac{\phi_s A_s}{F_s} \quad (4)$$

A plot of $F_{obs}/[u]_0$ vs $[u]_0$ was then used to determine $\phi_{u(monomer)}$. The linear analysis of $F_{obs}/[u]_0$ at the low concentration (2.50 × 10^{-4} mM to 6.00 × 10^{-4} mM) gave the value of $F_{obs}/[u]_0$ under $[u]_0 \to 0$ as the intercept. Then eq 4 was used to give the value of $\phi_{u(monomer)}$ as eq 5.

Linear fitting in Figure 7b and eq 4 thus gave

$$\phi_{u(monomer)} = (3.42 \pm 0.36) \times 10^{-4} \quad (5)$$

Accordingly, a value of $\phi_{u(monomer)}$ = 3.42 × 10^{-4} was used for the ensuing analyses. The error in the curve fitting is ca. 10% and was ignored in these latter calculations.

Considering elementary reactions i−iii, the following relationship could be derived as eq 6:

$$\frac{d[u^*]}{dt} = j_1[u] - j_2[u^*] - k_1[u^*] \quad (6)$$

A quasi-steady-state assumption was then made resulting in eq 7:

DOI: 10.1021/jacs.8b09021
J. Am. Chem. Soc. 2019, 141, 4597−4612

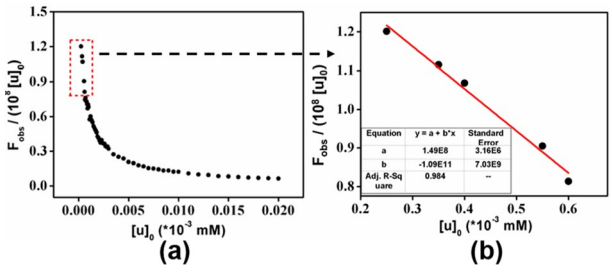

Figure 7. Plot of $F_{obs}/[u]_0$ vs $[u]_0$ (a) and expanded view of the plot for the data recorded at low concentrations showing the linear relationship (b).

$$\frac{d[u^*]}{dt} = [j_1 u] - j_2[u^*] - k_1[u^*] = 0 \quad (7)$$

This allowed a relationship between $\phi_{u(monomer)}$ and the parameters j_2 and k_1 to be expressed as eq 8:

$$\phi_{u(monomer)} = \frac{j_2}{j_2 + k_1} = (3.42 \pm 0.36) \times 10^{-4} \quad (8)$$

With the analysis at $[u]_0 \to 0$ complete, the monomer−dimeric excimer model was used to treat the experimental data for $0 \le [u]_0 \le 0.020$ mM. Toward this end, eqs 9 and 10 were derived based on the elementary reactions i−v as follows:

$$\frac{d[u^*]}{dt} = [j_1 u] - j_2[u^*] - k_1[u^*] - k_2[u^*][u] \quad (9)$$

$$\frac{d[u_2^*]}{dt} = k_2[u^*][u] - k_3[u_2^*] \quad (10)$$

As above, a quasi-steady-state assumption was made (eq 11):

$$\frac{d[u^*]}{dt} = \frac{d[u_2^*]}{dt} = 0 \quad (11)$$

Combining eqs 9−11 gave eq 12 as follows:

$$\frac{[u_2^*]}{[u^*][u]} = \frac{k_2}{k_3} = K_{dimer} \quad (12)$$

It was further assumed that the relationship between u, u*, and u_2* can be treated as a chemical equilibrium:

$$u^* + u \overset{K_{dimer}}{\rightleftharpoons} u_2^*$$

Meanwhile, eqs 13 and 14 were defined (note here $[u]_{all}$ is equal to $[u]_0$):

$$[u]_{monomer} = [u] + [u^*] \quad (13)$$

$$[u]_{monomer} + [2u_2^*] = [u]_{all} \quad (14)$$

Since u_2* is defined as non-fluorescent in this model per experimental observation (vide supra), the observed emission is from $u_{monomer}$ (i.e., ground- and excited-state forms of u^{2+}; see definitions above). Accordingly, eq 15 could be set up as follows:

$$\frac{F_{obs}}{A_{u(monomer)}\phi_{u(monomer)}} = \frac{F_s}{A_s\phi_s} \quad (15)$$

Equation 15 was then used to produce eq 16 as follows:

$$\frac{F_{obs}}{\varepsilon_u[u]_{monomer}l\,\phi_{u(monomer)}} = \frac{F_s}{A_s\phi_s} \quad (16)$$

Finally, the total concentration of monomeric u^{2+} ($[u]_{monomer}$) could be related to F_{obs} per eq 17:

$$[u]_{monomer} = \frac{F_{obs}}{\varepsilon_u\phi_{u(monomer)}l}\frac{A_s\phi_s}{F_s} \quad (17)$$

Equation 17 was used to generate eq 18:

$$[u_2^*] = [(u]_{all} - [u]_{monomer})/2 \quad (18)$$

Equations 11 and 13 were then used to derive eq 19:

$$[u] = \left(k_2[u]_{monomer} - j_1 - j_2 - k_1 + \sqrt{(k_2[u]_{monomer} - j_1 - j_2 - k_1)^2 + 4k_2(j_2 + k_1)[u]_{monomer}}\right)/2k_2 \quad (19)$$

Equations 9, 10, 13, and 19 were then considered simultaneously to obtain a relation between $[u_2^*]$ and $[u]_{monomer}$ in the form of eq 20:

$$\begin{aligned}[u_2^*] &= [f u]_{monomer} = K_{dimer}[u^*][u] = \\ &K_{dimer}[u]([u]_{monomer} - [u]) = \\ &K_{dimer}\left(k_2[u]_{monomer} - j_1 - j_2 - k_1 + \sqrt{(k_2[u]_{monomer} - j_1 - j_2 - k_1)^2 + 4k_2(j_2 + k_1)[u]_{monomer}}\right)/2k_2 \\ &\times \left(2k_2[u]_{monomer} - k_2[u]_{monomer} + j_1 + j_2 + k_1 - \sqrt{(k_2[u]_{monomer} - j_1 - j_2 - k_1)^2 + 4k_2(j_2 + k_1)[u]_{monomer}}\right)/2k_2 \end{aligned} \quad (20)$$

The parameters A, B, and C were set as follows:

$$A = k_2 \quad (21)$$

$$B = j_2 + k_1 \quad (22)$$

$$C = j_1 \quad (23)$$

Equation 20 could then be expressed as eq 24:

$$\begin{aligned}[u_2^*] &= [f u]_{monomer} = \\ &K_{dimer}\left(A[u]_{monomer} - B - C + \sqrt{(A[u]_{monomer} - B - C)^2 + 4AB[u]_{monomer}}\right)/2A \\ &\times \left(A[u]_{monomer} + B + C - \sqrt{(A[u]_{monomer} - B - C)^2 + 4AB[u]_{monomer}}\right)/2A \end{aligned} \quad (24)$$

From the observed emission intensity values (F_{obs}) of acetonitrile solutions containing different $[u]_{all}$, the $[u]_{monomer}$ term can be calculated from eq 17. This allows $[u_2^*]$ to be deduced through eq 18. A plot of $[u_2^*]$ vs $[u]_{monomer}$ could then be fitted in a nonlinear fashion using eq 24. Fixed values of the parameters of A = 4.47 × 10^7 M^{-1} s^{-1}, B = 1.68 s^{-1}, and C = 59.9 s^{-1} allowed the nonlinear fitting to be optimized (cf. Figure 8). This gave a calculated K_{dimer} value of (5.48 ± 0.12) × 10^6 M^{-1}, where the errors are the curve-fitting errors.

DOI: 10.1021/jacs.8b09021
J. Am. Chem. Soc. 2019, 141, 4597−4612

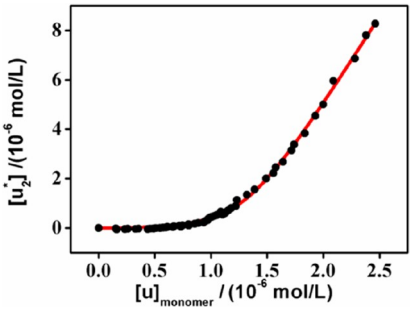

Figure 8. Plot of $[u_2^*]$ vs $[u]_{monomer}$ (black points). Shown in red is a nonlinear fitting of the data per eq 25.

From the result of the nonlinear fitting a series of relative parameter values j_1 = 59.9 s^{-1}, j_2 = 1.56 s^{-1}, k_1 = 4.55 × 10^{8} s^{-1}, k_2 = 4.47 × 10^{7} M^{-1} s^{-1}, and k_3 = 0.12 s^{-1} could be derived. Likewise, a relationship between $[u_2^*]$ and $[u]_{monomer}$ could be established per eq 25:

$$[u_2^*] = f([u]_{monomer}) = 3.57[u]_{monomer} + 5.21\times 10^{-6} - \sqrt{14.3[u]_{monomer})^2 - 3.71\times 10^{-5}[u]_{monomer} + 2.71\times 10^{-11}} \quad (25)$$

From these parameters and using the relationship embodied in eq 17, the simulated emission intensity (F_{sim}) could be calculated. This was then compared with the experimental F_{obs} values as shown in Figure 9.

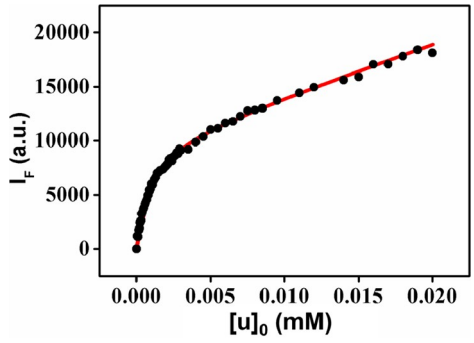

Figure 9. Plot of F_{obs} and F_{sim} vs $[u]_0$. Experimental points are shown in black, whereas the red line is a simulation made per eq 17.

Gratifyingly, a good match between the calculated curve and the experimental points was seen. Therefore, we believe that at least up to $[1^{2+}]$ = 0.020 mM contributions from possible higher order aggregated species (e.g., trimers or tetramers) can be largely ignored. Therefore, on the basis of eqs 10, 13, 14, and 25, the relationship between [u], $[u^*]$, $[u_2^*]$, and $[u]_0$ could be plotted in the form of a speciation diagram (cf. Figure 10 and SI).

Analysis of the Effect of Pyrophosphate Binding on the Fluorescence Features of $1^{2+}\cdot 2PF_6^-$ and Fit to a 1:1 Model. The key inference to be drawn from the above fitting efforts and the underlying experiments is that a disaggregation of the excimer form (or forms) will lead to an enhancement in the emission intensity. We thus considered it likely that species, such as oxoanions, that induced such disaggregation could be detected via changes in the emission intensity of $1^{2+}\cdot 2PF_6^-$. Accordingly, we set out to explore further the nature and the extent of the pyrophosphate-induced turn on

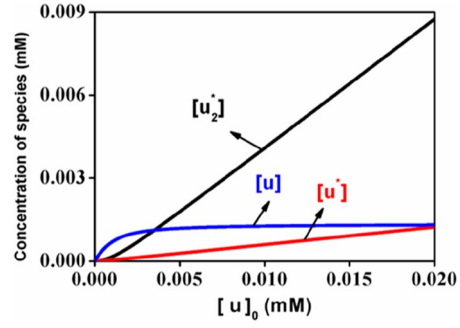

Figure 10. Plot of [u], $[u^*]$, and $[u_2^*]$ vs $[u]_0$.

fluorescent response noted above (cf. Figure 3 and accompanying discussion).

Concentration-dependent fluorescence studies of 1:1 or 1:10 mixtures containing $1^{2+}\cdot 2PF_6^-$ and $3TBA^+\cdot HP_2O_7^{3-}$ were carried out over the concentration range included in the analysis of the anion-free receptor solutions, namely $[1^{2+}\cdot 2PF_6^-]$ as 1.00 × 10^{-3} mM to 0.020 mM (λ_{ex} = 334 nm in acetonitrile for emission). In the case of 1:10 macrocycle to pyrophosphate ratio, the emission intensity shows a good linear relationship with $[1^{2+}\cdot 2PF_6^-]$. This was also true for the 1:1 mixture with the same emission intensity at every $[1^{2+}\cdot 2PF_6^-]$ provided that the $[1^{2+}\cdot 2PF_6^-]$ concentration was ≥0.010 mM.

The deviation seen for the 1:1 macrocycle to pyrophosphate samples at lower $1^{2+}\cdot 2PF_6^-$ concentrations could reflect a lack of full complexation, which would be expected to be essentially complete under the other conditions associated with this set of experiments (Figure 11a and SI). Supporting concentration-dependent UV−vis spectral studies of these 1:1 or 1:10 ($[1^{2+}\cdot 2PF_6^-]$/$[3TBA^+\cdot HP_2O_7^{3-}]$) mixtures revealed a good fit to the Beer−Lambert relationship (Figure 11b and SI). These findings are most easily interpreted in terms of the formation of a 1:1 thermostable complex, $1^{2+}\cdot HP_2O_7^{3-}$, over a limited concentration regime (i.e., ≥0.010 $[1^{2+}\cdot 2PF_6^-]$ ≤ 0.020 mM).

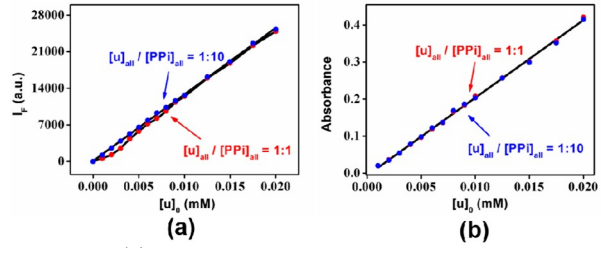

Figure 11. (a) Change in the emission intensity between 390 and 650 nm seen in the concentration-dependent fluorescent emission spectra of 1:1 (red •) and 1:10 (blue •) mixtures of $1^{2+}\cdot 2PF_6^-$ and $3TBA^+\cdot HP_2O_7^{3-}$ in acetonitrile where the concentration of 1^{2+} is varied from 1.00 × 10^{-3} mM to 0.020 mM. The excitation wavelength (λ_{ex}) was 334 nm. The black line corresponds to an associated linear fit (created via the linear expression $F_{obs(390-650\ nm)}$ = (1.3 ± 0.1) × 10^{3} $[1^{2+}]$ with an adjusted R^2 = 0.999) between the emission intensity and the concentration of 1^{2+}. Voltage = 400 V, entrance slit width = 5 nm, exit slit width = 10 nm. (b) Change in absorbance at 317 nm seen under conditions of concentration-dependent UV−vis spectral analysis of 1:1 (red •) and 1:10 (blue •) mixtures of $1^{2+}\cdot 2PF_6^-$ and $3TBA^+\cdot HP_2O_7^{3-}$ in acetonitrile where the concentration of 1^{2+} is varied from 1.00 × 10^{3} mM to 0.020 mM. The black line corresponds to a linear fit with an adjusted R^2 = 0.998 to a linear expression that assumes Beer−Lambert behavior, namely $Abs_{(319\ nm)}$ = (21.0 ± 0.2) × $[1^{2+}]$.

DOI: 10.1021/jacs.8b09021
J. Am. Chem. Soc. 2019, 141, 4597−4612

as long as the pyrophosphate anion is present at least 1 mol equiv.

Although it was appreciated that the above 1:1 monomer−dimeric excimer equilibrium model could not account for the full fluorescence spectral response when mixtures of $1^{2+}\cdot 2PF_6^-$ were treated with $3TBA^+\cdot HP_2O_7^{3-}$ in acetonitrile, it was considered a good starting point for a possible quantitative analysis. The following elementary reactions were thus considered in the context of an initial global kinetic analysis of the emission intensities observed at varying $[HP_2O_7^{3-}]/[1^{2+}]$ ratios:

$$u + h\nu_1 \xrightarrow{j_1} u^* \quad \text{(M-i)}$$

$$u^* \xrightarrow{j_2} u + h\nu_2 \quad \text{(M-ii)}$$

$$u^* + M \xrightarrow{k_1} u + M \quad \text{(M-iii)}$$

$$u^* + u \xrightarrow{k_2} u_2^* \quad \text{(M-iv)}$$

$$u_2^* + M \xrightarrow{k_3} u + u + M \quad \text{(M-v)}$$

$$u + \text{PPi} \xrightarrow{k_4} u\cdot\text{PPi} \quad \text{(M-vi)}$$

$$u\cdot\text{PPi} \xrightarrow{k_5} u + \text{PPi} \quad \text{(M-vii)}$$

$$u\cdot\text{PPi} + h\nu_1 \xrightarrow{j_3} (u\cdot\text{PPi})^* \quad \text{(M-viii)}$$

$$(u\cdot\text{PPi})^* \xrightarrow{j_4} u\cdot\text{PPi} + h\nu_3 \quad \text{(M-ix)}$$

$$(u\cdot\text{PPi})^* + M \xrightarrow{k_6} u\cdot\text{PPi} + M \quad \text{(M-x)}$$

where u, u^*, u_2^*, M, $h\nu_1$, and $h\nu_2$ are defined as before; PPi is $HP_2O_7^{3-}$; u·PPi is the thermostable 1:1 complex between 1^{2+} and PPi in the ground state; (u·PPi)* is the excited state of u·PPi under conditions of irradiation (λ_{ex} = 334 nm); and parameters j_1, j_2, k_1, k_2, k_3, k_4, k_5, j_3, j_4, and k_6 are rate constants corresponding to the individual (but inter-related) elementary reactions. Here, the effects of media (including solvent, acetonitrile, and counteranion, PF_6^-) are ignored, as are the potential contributions from higher order aggregates. It is thus assumed that the sole aggregation product of 1^{2+} (u) is the non-fluorescent dimeric excimer, u_2^*, and PPi is also considered as non-emissive.

The 1:10 (blue ●) data set corresponding to the plot of F_{obs} vs $[u]_0$ in Figure 11a that was used to determine $\phi_{u\cdot PPi}$. The value of $\phi_{u\cdot PPi}$ could then be expressed as eq M1:

$$\phi_{u\cdot\text{PPi}} = 1.493\times 10^{-2} \quad \text{(M1)}$$

Concentration-dependent UV−vis spectra of 1:10 (blue ●) mixtures containing $1^{2+}\cdot 2PF_6^-$ and $3TBA^+\cdot HP_2O_7^{3-}$ in acetonitrile used to determine the molar absorption coefficient of u·PPi ($\varepsilon_{u\cdot PPi}$) (cf. SI). The value of $\varepsilon_{u\cdot PPi}$ at 334 nm could then be expressed as eq M2:

$$\varepsilon_{u\cdot\text{PPi}} = 1.535\times 10^{4} \quad \text{(M2)}$$

Considering elementary reactions M-i−M-x and assuming quasi-steady-state kinetics, the following expressions were deduced:

$$\frac{d[u^*]}{dt} = [j_1\, u] - j_2[u^*] - k_1[u^*] - k_2[u^*][u] \quad \text{(M3)}$$

$$\frac{d[u_2^*]}{dt} = k_2[u^*][u] - k_3[u_2^*] \quad \text{(M4)}$$

$$\frac{d[(u\cdot\text{PPi})^*]}{dt} = j_3[u\cdot\text{PPi}] - j_4[(u\cdot\text{PPi})^*] - k_6[(u\cdot\text{PPi})^*] \quad \text{(M5)}$$

$$\frac{d[u\cdot\text{PPi}]}{dt} = k_4[u][\text{PPi}] - k_5[u\cdot\text{PPi}] - j_3[u\cdot\text{PPi}] + j_4[(u\cdot\text{PPi})^*] + k_6[(u\cdot\text{PPi})^*] \quad \text{(M6)}$$

$$\frac{d[u^*]}{dt} = \frac{d[u_2^*]}{dt} = \frac{d[(u\cdot\text{PPi})^*]}{dt} = \frac{d[u\cdot\text{PPi}]}{dt} = 0 \quad \text{(M7)}$$

The relationship between [u], [u*], $[u]_{monomer}$ and $[u_2^*]$ can be expressed in terms of $[u]_{monomer}$:

$$[u] = \left(k_2[u]_{monomer} - j_1 - j_2 - k_1 + \sqrt{(k_2[u]_{monomer} - j_1 - j_2 - k_1)^2 + 4k_2(j_2 + k_1)[u]_{monomer}}\right)/2k_2 \quad \text{(M8)}$$

$$[u^*] = \frac{j_1[u]}{j_2 + k_1 + k_2[u]} \quad \text{(M9)}$$

$$[u_2^*] = \frac{k_2}{k_3}[u][u^*] = K_{dimer}[u][u^*] = 3.57[u]_{monomer} + 5.21\times 10^{-6} - \sqrt{14.3[u]_{monomer})^2 - 3.71\times 10^{-5}[u]_{monomer} + 2.71\times 10^{-11}} \quad \text{(M10)}$$

Equation M11 may then be derived from eqs M5 and M7:

$$[(u\cdot\text{PPi})^*] = \frac{j_3}{j_4 + k_6}[u\cdot\text{PPi}] \quad \text{(M11)}$$

Combining eqs M5−M7 gives eq M12:

$$[u\cdot\text{PPi}] = \frac{k_4}{k_5}[u][\text{PPi}] \quad \text{(M12)}$$

Equation M12 may be rewritten as eq M13:

$$\frac{[u\cdot\text{PPi}]}{[u][\text{PPi}]} = \frac{k_4}{k_5} = K_{u\cdot\text{PPi}} \quad \text{(M13)}$$

Equation M13 implies that the relationship between u, PPi, and u·PPi can be expressed as a chemical equilibrium:

$$u + \text{PPi} \overset{K_{u\cdot\text{PPi}}}{\rightleftharpoons} u\cdot\text{PPi}$$

Here, $K_{u\cdot PPi}$ can be considered as the binding constant corresponding to the interaction between u and PPi. From mass balance and eq M11, eqs M14 and M15 may be defined:

$$[u\cdot\text{PPi}]_{all} = [u\cdot\text{PPi}] + [(u\cdot\text{PPi})^*] = \frac{j_3 + j_4 + k_6}{j_4 + k_6}[u\cdot\text{PPi}] \quad \text{(M14)}$$

$$\frac{j_3 + j_4 + k_6}{j_4 + k_6} = D_1 \quad \text{(M15)}$$

Equation M14 can be expressed as eq M16:

DOI: 10.1021/jacs.8b09021
J. Am. Chem. Soc. 2019, 141, 4597−4612

$$[u\cdot PPi]_{all} = D_1[u\cdot PPi] \quad (M16)$$

Combining with eq M13 gives eq M17:

$$\frac{[u\cdot PPi]_{all}}{[u][PPi]} = D_1 K_{u\cdot PPi} = K^*_{u\cdot PPi} \quad (M17)$$

Equation M17 implies that the relationship between u, PPi, and $(u\cdot PPi)_{all}$ may also be considered as a chemical equilibrium:

$$u + PPi \xrightarrow{K^*_{u\cdot PPi}} (u\cdot PPi)_{all}$$

It is noted that $K^*_{u\cdot PPi}$ is larger than $K_{u\cdot PPi}$.

More expressions that relate to these experiments are

$$[u]_{all} = [u]_{monomer} + [2u_2^*] + [u\cdot PPi]_{all} \quad (M18)$$

$$[PPi]_{all} = [u\cdot PPi]_{all} + [PPi] \quad (M19)$$

Thus,

$$[u\cdot PPi]_{all} = [u]_{all} - [u]_{monomer} - [2u_2^*] \quad (M20)$$

In this model, the fluorescent response only comes from the emission of $u_{(monomer)}$ and $[u\cdot PPi]_{all}$:

$$F_{obs} = \phi_{u\cdot PPi}\varepsilon_{u\cdot PPi}[u\cdot PPi]_{all} l \frac{F_s}{A_s\phi_s} + \phi_{u(monomer)}\varepsilon_{u(monomer)}[u]_{monomer} l \frac{F_s}{A_s\phi_s} \quad (M21)$$

From concentration-dependent fluorescence and UV−vis spectral studies of 1:10 ($[u]_{all}/[PPi]_{all}$) mixtures (Figure 11 and SI), eq M22 was obtained:

$$\Phi_1 = \phi_{u\cdot PPi}\varepsilon_{u\cdot PPi} l \frac{F_s}{A_s\phi_s} = 1.263\times 10^9 \quad (M22)$$

The previously described monomer−dimeric excimer equilibrium model without PPi gives eq M23:

$$\Phi_2 = \phi_{u(monomer)}\varepsilon_{u(monomer)} l \frac{F_s}{A_s\phi_s} = 3.862\times 10^7 \quad (M23)$$

The combination of elementary reaction M-x and eqs M20−M23 gives eq M24:

$$F_{obs} = \Phi_1[u\cdot PPi]_{all} + \Phi_2[u]_{monomer} = \Phi_1([u]_{all} - [u]_{monomer} - [2u_2^*]) + \Phi_2[u]_{monomer} = \Phi_1\left([u]_{all} - [u]_{monomer} - 2\left((3.57[u]_{monomer}) + 5.21\times 10^{-6} - \sqrt{14.23[u]_{monomer}^2 - 3.71\times 10^{-5}[u]_{monomer} + 2.71\times 10^{-11}}\right)\right) + \Phi_2[u]_{monomer} \quad (M24)$$

With $[u]_{all}$ and $[PPi]_{all}$ known, $[u]_{monomer}$ can be solved using the fluorescence spectral data (eq M24). Then, $[u_2^*]$ can be calculated from $[u]_{monomer}$ and eq M10, while $[u\cdot PPi]_{all}$ may be further calculated via eq M20. Thus, the value of [PPi] may be obtained using eq M25:

$$[PPi] = [PPi]_{all} - [u\cdot PPi]_{all} = [PPi]_{all} - ([u]_{all} - [u]_{monomer} - [2u_2^*]) \quad (M25)$$

Finally, $K^*_{u\cdot PPi}$ could be calculated using eq M26:

$$K^*_{u\cdot PPi} = \frac{[u\cdot PPi]_{all}}{[u][PPi]} \quad (M26)$$

The titration data from Figure 3 were then used as a check of eq M26. If the model is valid, the values of $K^*_{u\cdot PPi}$ should remain constant during the full course of the titration. However, it was found that the calculated values of $K^*_{u\cdot PPi}$ based on this model were not constant. Rather, they a peak value (2.18×10^8) was observed when $[PPi]_{all}/[u]_{all} = 1$.

It is possible that when $[PPi]_{all}/[u]_{all}$ is larger than 1, aggregation of PPi causes a decrease in $[u\cdot PPi]_{all}$, which is reflected in a smaller $K^*_{u\cdot PPi}$. Conversely, when the $[PPi]_{all}/[u]_{all}$ ratio is less than 1, PPi could have a direct effect on the dimeric excimer. When $[PPi]_{all}/[u]_{all}$ is around 1 the effect of these competing influences is minimized. To the extent such rationales are correct, the peak value (2.18×10^8) may approximate the true $K^*_{u\cdot PPi}$ value. For ease, this is summarized in the form of eq M27:

$$K^*_{u\cdot PPi} = 2.18\times 10^8 M^{-1} \quad (M27)$$

This result is graphed in Figure 12.

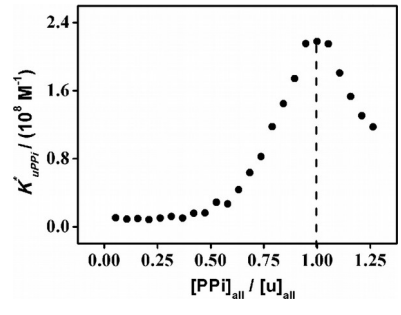

Figure 12. Values of $K^*_{u\cdot PPi}$ calculated using a simple 1:1 complexation analysis. A peak value of $2.18\times 10^8 M^{-1}$ was obtained when $[PPi]_{all}/[u]_{all} = 1$.

Mixed 2:1 and 1:1 (u/PPi) Complexation Analysis of Pyrophosphate Binding and Its Effect on the Fluorescence Features of $1^{2+}\cdot 2PF_6^-$. Although the above analyses highlight the fact that a "regime of reliability" can be found where a simple 1:1 complexation model can be made to fit the data, it is clear that such a treatment cannot account well for the fluorescence response seen over the course of the titration process involving treating acetonitrile solutions of $1^{2+}\cdot 2PF_6^-$ with $3TBA^+\cdot HP_2O_7^{3-}$. Thus, a mixed 2:1 and 1:1 (u/PPi) model was employed. For this global analysis, additional elementary reactions representing the putative interactions between u_2^* and PPi were considered:

$$u + h\nu_1 \xrightarrow{j_1} u^* \quad (D\text{-i})$$

$$u^* \xrightarrow{j_2} u + h\nu_2 \quad (D\text{-ii})$$

$$u^* + M \xrightarrow{k_1} u + M \quad (D\text{-iii})$$

$$u^* + u \xrightarrow{k_2} u_2^* \quad (D\text{-iv})$$

$$u_2^* + M \xrightarrow{k_3} u + u + M \quad (D\text{-v})$$

$$u + PPi \xrightarrow{k_4} u\cdot PPi \quad (D\text{-vi})$$

DOI: 10.1021/jacs.8b09021
J. Am. Chem. Soc. 2019, 141, 4597−4612

$$u\cdot\mathrm{PPi} \xrightarrow{k_5} u + \mathrm{PPi} \quad \text{(D-vii)}$$

$$u\cdot\mathrm{PPi} + h\nu_1 \xrightarrow{j_3} (u\cdot\mathrm{PPi})^* \quad \text{(D-viii)}$$

$$(u\cdot\mathrm{PPi})^* \xrightarrow{j_4} u\cdot\mathrm{PPi} + h\nu_3 \quad \text{(D-ix)}$$

$$(u\cdot\mathrm{PPi})^* + M \xrightarrow{k_6} u\cdot\mathrm{PPi} + M \quad \text{(D-x)}$$

$$u_2^* + \mathrm{PPi} \xrightarrow{k_7} u_2\cdot\mathrm{PPi} \quad \text{(D-xi)}$$

$$u_2\cdot\mathrm{PPi} \xrightarrow{k_8} u + u + \mathrm{PPi} \quad \text{(D-xii)}$$

where u, u^*, u_2^*, M, $h\nu_1$, $h\nu_2$, $h\nu_3$, PPi, u·PPi, and $(u\cdot\mathrm{PPi})^*$ are defined as before. u_2·PPi is the thermostable 1:1 complex between u_2^* and PPi. u_2^* and PPi are considered as non-emission, as is u_2·PPi. Parameters j_1, j_2, k_1, k_2, k_3, k_4, k_5, j_3, j_4, k_6, k_7, and k_8 are rate constants for the individual (but interrelated) elementary reactions. As in the case of the initial simplified 1:1 model above, the effects of media (M) are ignored, as are the potential effects of higher order aggregates.

Considering elementary reactions D-i−D-xii with a quasi-steady-state assumption, the following expressions may be deduced:

$$\frac{d[u^*]}{dt} = [j_1 u] - j_2[u^*] - k_1[u^*] - k_2[u^*][u] \quad \text{(D1)}$$

$$\frac{d[u_2^*]}{dt} = k_2[u^*][u] - k_3[u_2^*] - k_7[u_2^*][\mathrm{PPi}] \quad \text{(D2)}$$

$$\frac{d[(u\cdot\mathrm{PPi})^*]}{dt} = j_3[u\cdot\mathrm{PPi}] - j_4[(u\cdot\mathrm{PPi})^*] - k_6[(u\cdot\mathrm{PPi})^*] \quad \text{(D3)}$$

$$\frac{d[(u\cdot\mathrm{PPi})]}{dt} = k_4[u][\mathrm{PPi}] - k_5[u\cdot\mathrm{PPi}] - j_3[u\cdot\mathrm{PPi}] + j_4[(u\cdot\mathrm{PPi})^*] + k_6[(u\cdot\mathrm{PPi})^*] \quad \text{(D4)}$$

$$\frac{d[(u_2\cdot\mathrm{PPi})]}{dt} = k_7[u_2^*][\mathrm{PPi}] - k_8[u_2\cdot\mathrm{PPi}] \quad \text{(D5)}$$

$$\frac{d[u^*]}{dt} = \frac{d[u_2^*]}{dt} = \frac{d[(u\cdot\mathrm{PPi})^*]}{dt} = \frac{d[(u\cdot\mathrm{PPi})]}{dt} = \frac{d[(u_2\cdot\mathrm{PPi})]}{dt} = 0 \quad \text{(D6)}$$

Here, the relationship between $[u^*]$, $[u]_{monomer}$, and $[u_2^*]$ is defined via eqs D7−D11:

$$[u^*] = \frac{j_1[u]}{j_2 + k_1 + k_2[u]} \quad \text{(D7)}$$

$$[u_2^*] = \frac{k_2[u^*][u]}{k_3 + k_7[\mathrm{PPi}]} \quad \text{(D8)}$$

$$[(u\cdot\mathrm{PPi})^*] = \frac{j_3[u\cdot\mathrm{PPi}]}{j_4 + k_6} \quad \text{(D9)}$$

$$[u\cdot\mathrm{PPi}] = \frac{k_4}{k_5}[u][\mathrm{PPi}] \quad \text{(D10)}$$

$$[u_2\cdot\mathrm{PPi}] = \frac{k_7}{k_8}[u_2^*][\mathrm{PPi}] \quad \text{(D11)}$$

Equation D11 may be rewritten as eq D12:

$$\frac{[u_2\cdot\mathrm{PPi}]}{[u_2^*][\mathrm{PPi}]} = \frac{k_7}{k_8} = K_{u_2\cdot\mathrm{PPi}} \quad \text{(D12)}$$

Equation D12 implies that the relationship between u_2^*, PPi, and u_2·PPi can be treated as a chemical equilibrium:

$$u_2^* + \mathrm{PPi} \underset{k_{-7}}{\overset{K_{u_2\cdot\mathrm{PPi}}}{\rightleftharpoons}} u_2\cdot\mathrm{PPi}$$

More expressions related to the experiments include the following:

$$[u]_{all} = [u]_{monomer} + [2u_2^*] + [u\cdot\mathrm{PPi}] + [2u_2\cdot\mathrm{PPi}] \quad \text{(D13)}$$

$$[\mathrm{PPi}]_{all} = [\mathrm{PPi}] + [u\cdot\mathrm{PPi}]_{all} + [u_2\cdot\mathrm{PPi}] \quad \text{(D14)}$$

In this model, the fluorescent response comes only from the emission contributions of $[u]_{monomer}$ and $[u\cdot\mathrm{PPi}]_{all}$:

$$F_{obs} = \Phi_1[u\cdot\mathrm{PPi}]_{all} + \Phi_2[u]_{monomer} \quad \text{(D15)}$$

where Φ_1 and Φ_2 are defined as per eqs M22 and M23. Assuming that PPi is completely bound to u during the titration process, the maximum fluorescence response may be expressed per eq D16:

$$F_{max} = \Phi_1[\mathrm{PPi}]_{all} + \Phi_2[u]_{monomer}, \quad \text{when } [u]_{all} \geq [\mathrm{PPi}]_{all} = [u\cdot\mathrm{PPi}]_{all}$$

or

$$F_{max} = \Phi_1[u]_{all}, \quad \text{when } [\mathrm{PPi}]_{all} > [u]_{all} = [u\cdot\mathrm{PPi}]_{all} \quad \text{(D16)}$$

The minimum fluorescence response when no binding between PPi and u occurs is expressed by eq D17:

$$F_{min} = [Fu]_{monomer,0} \quad \text{(D17)}$$

where $[u]_{monomer,0}$ is defined as the concentration of $[u]_{monomer}$ before addition of PPi. The range of fluorescence intensity values for $[u\cdot\mathrm{PPi}]_{all}$ is thus

$$F_{obs} - F_{min} \leq F_{obs} - \Phi_2[u]_{monomer} \leq F_{max} - \Phi_2[u]_{monomer} \quad \text{(D18)}$$

This gives eqs D19 and D20 for the lower bound of $[u\cdot\mathrm{PPi}]_{all}$ and the upper bound of $[u\cdot\mathrm{PPi}]_{all}$:

$$\Phi_1[u\cdot\mathrm{PPi}]_{min} = F_{obs} - F_{min} \quad \text{(D19)}$$

$$\Phi_1[u\cdot\mathrm{PPi}]_{max} = F_{max} - \Phi_2[u]_{monomer} \leq F_{max} \quad \text{(D20)}$$

with a range for $[u\cdot\mathrm{PPi}]_{all}$ of

$$\frac{F_{obs} - F_{min}}{\Phi_1} = [u\cdot\mathrm{PPi}]_{min} \leq [u\cdot\mathrm{PPi}]_{all} \leq [u\cdot\mathrm{PPi}]_{max} \leq \frac{F_{max}}{\Phi_1} \quad \text{(D21)}$$

For mixtures of $[u]_{all}$ and $[\mathrm{PPi}]_{all}$, we can calculate the relative concentration of the constituent species with a definite value of $[u\cdot\mathrm{PPi}]_{all}$ according to the following equations:

$$[u]_{monomer} = \frac{F_{obs} - \Phi_1[u\cdot\mathrm{PPi}]_{all}}{\Phi_2} \quad \text{(D22)}$$

DOI: 10.1021/jacs.8b09021
J. Am. Chem. Soc. 2019, 141, 4597−4612

$$[u] = \left(k_2[u]_{monomer} - j_1 - j_2 - k_1 + \sqrt{(k_2[u]_{monomer} - j_1 - j_2 - k_1)^2 + 4k_2(j_2 + k_1)[u]_{monomer}}\right) / 2k_2 \quad \text{(D23)}$$

$$[u^*] = \frac{j_1[u]}{j_2 + k_1 + k_2[u]} \quad \text{(D24)}$$

$$[PPi] = \frac{[u\cdot PPi]_{all}}{[u]K^*_{u\cdot PPi}} \quad \text{(D25)}$$

$$[u_2\cdot PPi] = [PPi]_{all} - [PPi] - [u\cdot PPi]_{all} \quad \text{(D26)}$$

$$[u_2^*] = \frac{1}{2}([u]_{all} - [u]_{monomer} - [u\cdot PPi]_{all} - [2u_2\cdot PPi]) = \frac{k_2[u][u^*]}{k_3 + k_7[PPi]} \quad \text{(D27)}$$

If we do not consider the dissociation of PPi from u_2^*, $[u_2^*]'$ can be expressed as eq D28:

$$[u_2^*]' = \frac{k_2[u][u^*]}{k_3} \quad \text{(D28)}$$

The following inequality expression could then be used to judge the reasonableness of the resulting calculated values:

$$[u_2^*] = \frac{k_2[u][u^*]}{k_3 + k_7[PPi]} < \frac{k_2[u][u^*]}{k_3} = [u_2^*]' \quad \text{(D29)}$$

Finally, $K_{u_2\cdot PPi}$ and k_7 are calculated via eqs D30 and D31:

$$K_{u_2\cdot PPi} = \frac{[u_2\cdot PPi]}{[PPi][u_2^*]} \quad \text{(D30)}$$

$$k_7 = \frac{k_2[u][u^*]}{[u_2^*][PPi]} - \frac{k_3}{[PPi]} \quad \text{(D31)}$$

For each titration point, the values of $[u]_{all}$ and $[PPi]_{all}$ are known. Therefore, F_{max} and F_{min} can be calculated using eqs D16 and D17, respectively. Meaningful values of $[u\cdot PPi]_{all}$ were then obtained using the limitations set by eq D21. The full range of $[u\cdot PPi]_{all}$ values was truncated into 400 equal regimes, and $[u\cdot PPi]_{all}$ was considered for each subset. For each, the relative concentration of the constituent species was calculated according to eqs D22−D27. Equation D29 was then used as criterion to evaluate which of the resulting calculated concentration values were meaningful. Using the resulting subset of calculated concentrations, the corresponding $K_{u_2\cdot PPi}$ and k_7 values were obtained from eqs D30 and D31. At each titration point, a range of $K_{u_2\cdot PPi}$ (the black line shown in Figure 13a) and k_7 values (the black line shown in Figure 13b) were calculated using the meaningful set of $[u\cdot PPi]_{all}$ values and corresponding concentration values (Figure 13 and SI).

The above analysis is predicated on the assumption that the values of $K_{u_2\cdot PPi}$ and k_7 are constant and do not vary, not only during a given titration, but also for titrations carried out using different initial Al^{3+}:$2PF_6^-$ concentrations. This implies that the calculated values (or range of meaningful values) for $K_{u_2\cdot PPi}$ and k_7 should be the same or nearly the same at all or, at least, most titration points in any given titration. Per this caveat, a set of $K_{u_2\cdot PPi}$ and k_7 values that provides the best fit for the entire

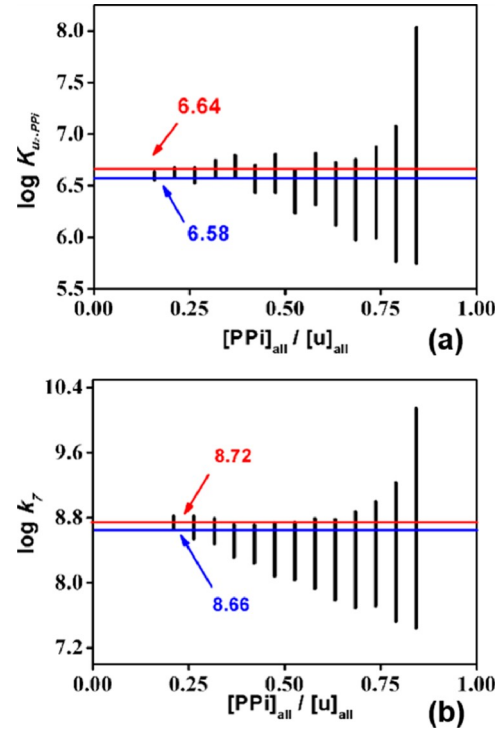

Figure 13. Range of $K_{u2\cdot PPi}$ (a) and k_7 values (b) calculated from a mixed 2:1 and 1:1 (u/PPi) complexation analysis. On this basis, log $K_{u_2\cdot PPi}$ values between 6.58 and 6.64, combined with log k_7 values between 8.66 and 8.72, are considered as providing the best overall match to the data. The black lines show the calculated range of $K_{u_2\cdot PPi}$ (a) and k_7 (b) values corresponding to each titration point. The values between the blue (lower bound) and red (upper bound) lines show the meaningful value ranges for $K_{u_2\cdot PPi}$ (a) and k_7 (b) derived by fitting the titration data to a mixed 2:1 and 1:1 (u/PPi) models as detailed more fully in the text.

process was selected. These values fall between the blue line (lower bound) and the red line (upper bound) shown in Figure 13a, but it should be noted that results from two limiting cases, namely the titration points with $[PPi]_{all}/[u]_{all} \rightarrow 0$ and $[PPi]_{all}/[u]_{all} \rightarrow 1$, were not taken into consideration. The concentration values of the species containing PPi ($[PPi]_{all}$, $[u\cdot PPi]_{all}$, and $[u_2\cdot PPi]$) are small such that the calculation of $K_{u_2\cdot PPi}$ and k_7 is unreliable when $[PPi]_{all}/[u]_{all} \rightarrow 0$. In the case of $[PPi]_{all}/[u]_{all} \rightarrow 1$, the small values of $[u_2\cdot PPi]$ likewise give rise to values for $K_{u_2\cdot PPi}$ and k_7 that are unreliable.

On this basis, the following $K_{u_2\cdot PPi}$ and k_7 values were selected:

$$K_{u_2} = 10^{6.61 \pm 0.03} M^{-1} = (4.08 \pm 0.17) \times 10^6 M^{-1} \quad \text{(D32)}$$

$$k_7 = 10^{8.69 \pm 0.03} s^{-1} = (4.91 \pm 0.34) \times 10^8 s^{-1} \quad \text{(D33)}$$

In order to test the validity of the above analysis, a series of concentration-dependent fluorescent spectral titrations were carried out. Calculated $K^*_{u\cdot PPi} = 2.18 \times 10^6 M^{-1}$, $K_{u_2\cdot PPi} = 4.08 \times 10^6 M^{-1}$, and $k_7 = 4.91 \times 10^8 s^{-1}$ values were used for simulated emission intensity calculations. For every given concentration of $[u]_{all}$ and $[PPi]_{all}$, solving eqs D34−D38 and eqs D13 and D14 provided simulated concentration values corresponding to a given specific titration datum point:

DOI: 10.1021/jacs.8b09021
J. Am. Chem. Soc. 2019, 141, 4597−4612

$$[u^*] = \frac{j_1[u]}{j_2 + k_1 + k_2[u]} = \frac{59.9[u]}{4551.6 + 4.47\times 10^7[u]} \quad \text{(D34)}$$

$$[u]_{monomer} = [u] + [u^*] = \frac{4.47\times 10^7[u]^2 + 4611.5[u]}{4551.6 + 4.47\times 10^7[u]} \quad \text{(D35)}$$

$$[u\cdot PPi]_{all} = K^*_{u\cdot PPi}[u][PPi] = 2.18\times 10^8[u][PPi] \quad \text{(D36)}$$

$$[u_2^*] = \frac{k_2[u][u^*]}{k_3 + k_7[PPi]} = 2.68\times 10^9[u]^2/(2.19\times 10^{16}[u][PPi] + 5.36\times 10^6[u] + 2.23\times 10^{12}[PPi] + 546.2) \quad \text{(D37)}$$

$$[u_2\cdot PPi] = K_{u_2\cdot PP}[u_2^*][PPi] = 1.09\times 10^{16}[u]^2[PPi]/(2.19\times 10^{16}[u][PPi] + 5.36\times 10^6[u] + 2.23\times 10^{12}[PPi] + 546.2) \quad \text{(D38)}$$

Using the calculated values of $[u\cdot PPi]_{all}$ and $[u]_{monomer}$, a series of emission intensity values that match the titration process could be found via eq D15; these were then compared with the measured values. Fluorescence emission spectra of a solution containing $1^{2+}\cdot 2PF_6^-$ (0.020 mM) in CH_3CN treated with increasing $HP_2O_7^{3-}$ concentrations (TBA^+ salt; from 0 to 0.026 mM) as per Figure 3, as well as titrations at $[1^{2+}\cdot 2PF_6^-]$ = 0.005 mM, were used to verify the model and are shown in Figure 14. Data from a number of other titrations of $[1^{2+}\cdot 2PF_6^-]$ ≤ 0.020 mM) were also used to verify the model (cf. SI). All of the experimental titration data sets proved consistent with the simulated values (the adjusted R^2 values were found to lie between 0.999 and 0.997). On this basis, we suggest that the mixed 2:1 and 1:1 (u/PPi) binding model proposed above provides a reasonable basis for quantifying the EDIE effects seen when macrocycle 1^{2+} is treated with the pyrophosphate anion under conditions of photoexcitation.

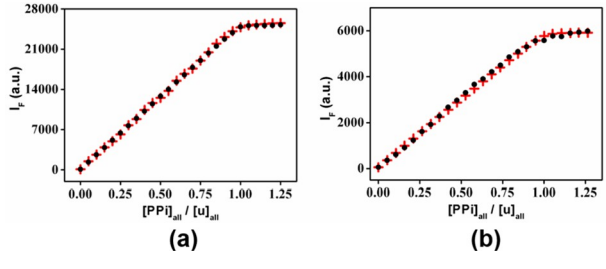

Figure 14. Experimental data obtained from EDIE experiments carried out at (a) 0.020 mM and (b) 0.005 mM in 1^{2+} are given as black points while the simulated values calculated per eq D15 are shown as red crosses. Other simulated I_{obs} values were also calculated; they are tabulated in the SI. The adjusted R^2 values were 0.999 for (a) and 0.998 for (b).

EDIE-Based Anion Sensing and Underlying Assumptions. To explore the selectivity of 1^{2+} as a turn on fluorescence probe for other anions, analogous fluorescence titrations of $1^{2+}\cdot 2PF_6^-$ (0.020 mM) in acetonitrile (λ_{ex} = 334 nm) were carried out with three other oxoanions: HCO_3^- and HSO_4^- as their respective TBA^+ salts; HCO_3^- as its TEA^+ salt). A strong response (fluorescence turn-on) was seen in the case of $H_2PO_4^-$ (cf. Figure S32). A less effective, but still notable, response was seen in the case of HCO_3^- (cf. Figure S33). In contrast to what was seen in the case of $HP_2O_7^{3-}$, where a 1:1 complex dominates in the presence of excess guest, curve fits to the titration results were consistent with a 1:2 (H:G) binding stoichiometry in the case of $H_2PO_4^{2-}$ and HCO_3^-. Support for this suggestion came from mass spectrometric studies (cf. Table S4), as well as from solid-state structural analyses (vide infra).

Little, if any, increase in the fluorescence intensity was seen when analogous titrations were carried out using a variety of other anions (i.e. HSO_4^-, SCN^-, N_3^-, F^-, Cl^-, Br^-, and I^-; all as their respective TBA^+ salts). In the case of $TBANO_3$, little immediate response was seen upon treatment with 100 molar equiv. However, when an initial 0.020 mM acetonitrile solution of $1^{2+}\cdot 2PF_6^-$ was treated with a large excess of NO_3^- (100 mM), the fluorescence intensity was seen to increase over the course of roughly 90 min (Figure S52). This finding is ascribed to the nitrate anion being a weak competitive inhibitor that is able to disaggregate the excimer of 1^{2+}. That this process occurs slowly could reflect what are presumably poor binding thermodynamics. In fact, the K_a corresponding to the interaction between 1^{2+} and NO_3^- proved too small to measure reliably (see discussion below).

A series of competition studies were then undertaken with $[1^{2+}\cdot 2PF_6^-]$ = 0.020 mM in CH_3CN and λ_{ex} = 334 nm (cf. Figure 15 and the SI). These revealed little effect on the maximal fluorescence intensity when titrations with $HP_2O_7^{3-}$ or $H_2PO_4^-$ were carried out in in the presence of a large excess of SCN^-, N_3^-, F^-, Cl^-, Br^-, I^-, or NO_3^-; again, 1^{2+} was found to function as a good "turn-on" fluorescence sensor for $HP_2O_7^{3-}$ (and $H_2PO_4^-$), the presence of these potential interferants notwithstanding. However, it is important to note that the $HP_2O_7^{3-}$ and $H_2PO_4^-$ were cross-competitive and acted as interferants for one another under these standard titration conditions (cf. SI).

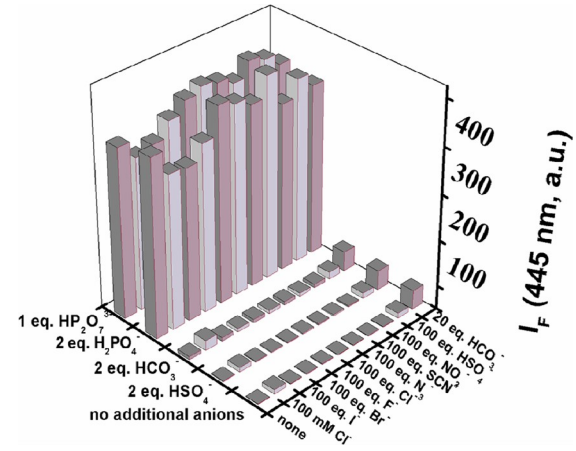

Figure 15. Anion induced immediate fluorescence response seen immediately after mixing $1^{2+}\cdot 2PF_6^-$ (0.020 mM) in CH_3CN (λ_{ex} = 334 nm) with the indicated anions. Note: The use of 100 molar equiv of HCO_3^- (2.00 mM) was found to induce precipitation. Therefore, only 20 equiv were used in these studies. Except for HCO_3^- (used as its tetraethylammonium salt, TEA^+), all anions were studied as their respective TBA^+ salts.

From the UV−vis titrations with $[1^{2+}]$ = 0.005 mM (for the $HP_2O_7^{3-}$) and 0.020 mM (for the other tested anions), K_{a1}

DOI: 10.1021/jacs.8b09021
J. Am. Chem. Soc. 2019, 141, 4597−4612

Table 2. Interactions between 1^{2+} and Anionic Species in Acetonitrile at 298 K[a,f]

guest	[H]/[G]	K_a		
		UV−vis	ITC[a]	fluorescence
$HP_2O_7^{3-}$	2:1	–	–	$(4.1 \pm 0.2) \times 10^6$ M^{-1}
	1:1	$(4.7 \pm 0.1) \times 10^6$ M^{-1}	$(1.3 \pm 0.1) \times 10^6$ M^{-1}	$(2.2 \pm 0.2) \times 10^8$ M^{-1}
$H_2PO_4^-$	1:1[b]	$(2.3 \pm 0.1) \times 10^6$ M^{-1}	$(2.0 \pm 0.2) \times 10^5$ M^{-1}	–[g]
	1:2[c]	$(4.7 \pm 0.1) \times 10^{13}$ M^{-2} [e]	$(2.0 \pm 0.2) \times 10^{10}$ M^{-2}	–[g]
HCO_3^-	1:1[b]	$(1.2 \pm 0.1) \times 10^3$ M^{-1}	–	–[g]
	1:2[c]	$(9.9 \pm 0.1) \times 10^6$ M^{-2}		–[g]
HSO_4^-	1:2	–	–	–
other tested anions[d]	–	–	–	–

[a] ITC titrations were carried out under higher concentrations and yielded smaller K_{a2} values compared with the results from UV−vis and fluorescence titrations. This is ascribed to the effect of aggregation. [b] Equilibrium (a) [H] + [G] ⇌ [HG] and (c) [HG] + [G] ⇌ [H_2G_2]. [c] K_{a1} for [HG]. [d] Other tested anions include NO_3^-, SCN^-, N_3^-, F^-, Cl^-, Br^-, and I^-, all as their TBA^+ salts. [e] It is noteworthy that a higher value for K_{a2}/K_{a1} larger than K_{a1} is seen in the case of $H_2PO_4^-$ and HCO_3^- under standard titration conditions ($[1^{2+}]$ = 0.020 mM) as determined from UV−vis spectroscopic titrations. This finding provides additional support for the proposed 1:2 binding mode, which may benefit from positive homotropic allostery.[24] [f] All errors are fitting errors. [g] Fluorescence spectroscopic titrations of $H_2PO_4^-$ and HCO_3^- appear to involve more complicated processes. Currently, we are unable to calculate K_{a1} and K_{a2} values reliably from the emission data.

values corresponding to the formation of 1:1 complex could be derived for several of the oxoanions and were found to follow the order $HP_2O_7^{3-}$ > $H_2PO_4^-$ ≫ HCO_3^- > HSO_4^-. In the case of NO_3^-, SCN^-, N_3^-, F^-, Cl^-, Br^-, and I^- the binding thermodynamics proved too small to quantify. For the 1:2 (receptor:anion) complexes, the K_{a2} order was found to be $H_2PO_4^-$ ≫ HCO_3^- > HSO_4^- (see Table 2 and the SI).

The K_a values calculated on the basis of UV−vis spectroscopic titrations assuming a 1:1 (H/G) binding model for $HP_2O_7^{3-}$ and mixed 1:1 and 1:2 model for $H_2PO_4^-$ and HCO_3^- (cf. SI). In the case of $HP_2O_7^{3-}$ and $H_2PO_4^-$ it proved possible to obtain concordant K_a (for $HP_2O_7^{3-}$) or K_{a1} (for $H_2PO_4^-$) values via ITC analyses even though higher concentrations were used and the effects of higher order aggregation could not be discounted. The values from these independent studies are included in Table 2. It is important to note that these measurements are probing ground-state interactions not EDIE per se.

Interactions between 1^{2+} and Anionic Guests in the Solid State. To obtain further insights into the presumed interactions between 1^{2+} and various anions, efforts were made to obtain a series of single crystals suitable for X-ray diffraction analysis. Toward this end, solutions of anion exchange products in a mixture of water/acetonitrile (1:1, v/v), water/(N,N-dimethylformamide (DMF), 1:1, v/v), or water/dioxane (1:1, v/v) were subject to slow evaporation. This allowed crystal structures of [1^{2+}·$H_2P_2O_7^{2-}$·4H_2O], [1^{2+}·2$H_2PO_4^-$·7.5H_2O], [1^{2+}·2HCO_3^-·dioxane·2H_2O], and [1^{2+}·2HSO_4^-·1.5CH_3CN] to be solved (see below and the SI). The structure of the pyrophosphate complex was presented previously and taken as initial evidence that treatment of 1^{2+} with $H_2P_2O_7^{2-}$ would induce disaggregation of excimer (cf. Figure 4e and accompanying discussion). The other anion-containing structures are discussed below.

The solid-state structure of 1^{2+}·2$H_2PO_4^-$·7.5H_2O revealed a 1:2 receptor:anion stoichiometry consistent with what was inferred from the solution-state studies discussed above (Figure 16). The phosphate anions exist in the form of a

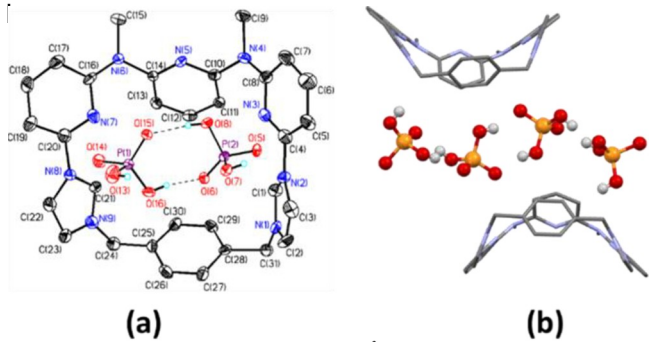

Figure 16. Single-crystal structure of 1^{2+}·2$H_2PO_4^-$·7.5H_2O showing (a) the interactions between 1^{2+} and the bound $H_2PO_4^-$ anions and (b) a side view shown in stick form showing the anion cluster that serves to separate individual units of 1^{2+}.

cluster that, based on the metric parameters, is stabilized by O−H hydrogen bonds between neighbor anions, charged and neutral C−H hydrogen bonds between the imidazolium and benzene ring(s) of 1^{2+}, respectively, and O atoms present in the anion cluster, as well as anion−π interactions, may also play a role in stabilizing the overall structure. A key point is that in this complex, as true for the pyrophosphate anion complex, little evidence of close receptor−receptor contact is seen. The contrast with the anion-free forms (cf. Figure 4a−d) is noteworthy and provides support for the suggestion that the solution-phase binding of $HP_2O_7^{3-}$ will serve to break up the excimer forms of 1^{2+}.

The structure of the [1^{2+}·2HCO_3^-·dioxane·2H_2O] complex revealed a 1:2 receptor: anion stoichiometry, a finding corresponding to the result of a solution-phase Job plot (cf. SI). In the solid state, two HCO_3^- molecular anions interact to form a dimeric structure $(HCO_3)_2^-$. This subunit is stabilized via two hydrogen bonds involving neighboring HCO_3^- units. One of the HCO_3^- anions is complexed directly with 1^{2+} and is held via C−H interactions involving 1^{2+} and an O atom of the bound HCO_3^- anion, even though this substrate fills only part

DOI: 10.1021/jacs.8b09021
J. Am. Chem. Soc. 2019, 141, 4597−4612

of the core (cf. Figure 17a,b and SI). Interestingly, examples of structurally characterized imidazolium-based HCO_3^- com-

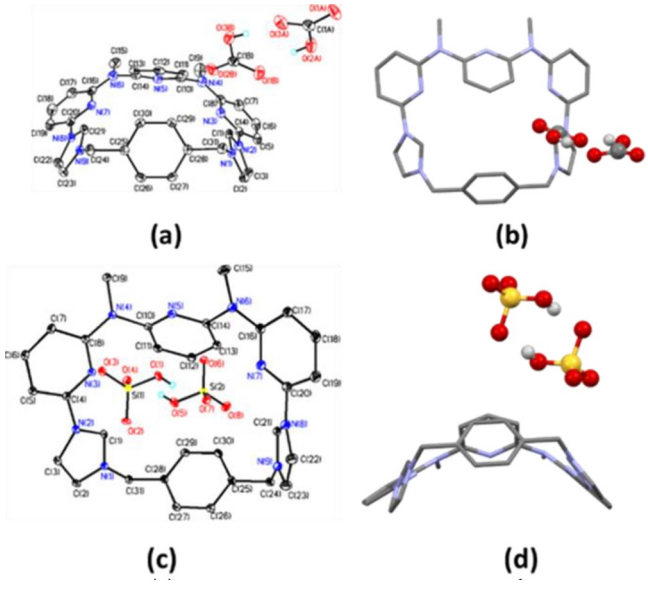

Figure 17. (a) Single-crystal structure of $1^{2+}\cdot 2HCO_3^-\cdot$dioxane$\cdot 2H_2O$ showing the binding interactions involving 1^{2+} and the HCO_3^- anions. (b) Top view of $1^{2+}\cdot 2HCO_3^-\cdot$dioxane$\cdot 2H_2O$ shown in stick form. (c) Single-crystal structure of $1^{2+}\cdot 2HSO_4^-\cdot 1.5CH_3CN$ showing the interactions involving 1^{2+} and the HSO_4^- anions. (d) Top view of $1^{2+}\cdot 2HSO_4^-\cdot 1.5CH_3CN$ shown in stick form.

plexes are limited.[25] Thus, this structure may contribute to our understanding of the design features needed to recognize this all-important anion.

The structure of $1^{2+}\cdot 2HSO_4^-\cdot 1.5CH_3CN$ was also solved. It revealed binding modes similar to those seen in the case of the HCO_3^- complex; again, one of two HSO_4^- anions present in a dimeric anion pair (i.e. $(HSO_4^-)_2$) also interacts with 1^{2+} via what are presumed to be strong hydrogen-bonding interactions (cf. Figures 17c,d). As above, the presence of the hydrogen-bonded anions may reflect a reduced propensity to stabilize a dimer form capable of forming an excimer under solution-phase conditions.

CONCLUSION

In summary, we describe here the use of an excimer disaggregation-induced emission (EDIE) strategy for the "turn-on" solution-phase fluorescence-based detection of $HP_2O_7^{3-}$ and $H_2PO_4^-$ oxoanions. The system relies on the use of a pyridine imidazolium-based anion receptor $1^{2+}\cdot 2PF_6^-$ that displays little propensity to aggregate in the ground state, which forms a poorly fluorescent excimer in acetonitrile solution. The $HP_2O_7^{3-}$, $H_2PO_4^-$, and to a lesser extent HCO_3^-, anions are effective at breaking up these aggregated species. This leads to production of fluorescent monomeric anion complexes whose structure precludes efficient aggregation. Other anions produce little response. As a result, good selectivity is observed. For instance, 0.02 mM acetonitrile solutions of $1^{2+}\cdot 2PF_6^-$ can be used to detect $HP_2O_7^{3-}$ efficiently even in the presence of 100 mM Cl^-. This selectivity is reflected in the calculated affinity constants. For instance, $K_a(HP_2O_7^{3-}):K_a(Cl^-) > 10000$. Support for the proposed EDIE mechanism came from single-crystal X-ray diffraction studies that revealed break up of dimerized anion-free solid-state structures in the presence of various anions. On the basis of the results presented here, we propose that disaggregation-based strategies involving excited-state species may have a role to play in the design of new sensor systems.

ASSOCIATED CONTENT

* Supporting Information

The Supporting Information is available free of charge on the ACS Publications website at DOI: 10.1021/jacs.8b09021.

Experimental details, UV−vis and NMR spectroscopic analyses, ESI-MS results, data fitting, and single-crystal X-ray diffraction studies, including Figures S1−S62 and Tables S1−S5 (PDF)

Calculated values for the parameters $[u]_0$, $[u_2^*]$, $[u]_{monomer}$, $[u^*]$, $[u]$, and $[u_0]/([u]+[u^*])$ (PDF)

X-ray crystallographic data for $1^{2+}\cdot 2H_2PO_4^-\cdot 7.5H_2O$ (CIF)

$1^{2+}\cdot 2HCO_3^-\cdot$dioxane$\cdot 2H_2O$ (CIF)

$1^{2+}\cdot H_2P_2O_7^{2-}\cdot 4H_2O$ (CIF)

$1^{2+}\cdot 2HSO_4^-\cdot 1.5CH_3CN$ (CIF)

$1^{2+}\cdot 2PF_6^-\cdot 2CH_3CN\cdot 0.25H_2O$ (CIF)

$1^{2+}\cdot 2PF_6^-\cdot$dioxane (CIF)

AUTHOR INFORMATION

Corresponding Authors

*sessler@cm.utexas.edu

*hanyuangong@bnu.edu.cn

ORCID

Jonathan L. Sessler: 0000-0002-9576-1325

Han-Yuan Gong: 0000-0003-4168-7657

Notes

The authors declare no competing financial interest.

ACKNOWLEDGMENTS

H.-Y. G. is grateful to the National Natural Science Foundation of China (21472014 and 21672025), National Basic Research Program of China (973 Program 2015CB856502), Young One-Thousand-Talents Scheme, the Fundamental Research Funds for the Central Universities, the Beijing Municipal Commission of Education, the Beijing National Laboratory for Molecular Science (BNLMS), and Beijing Normal University for financial support. Support from Shanghai University and the Robert A. Welch Foundation (F-0018) is also gratefully acknowledged.

REFERENCES

(1) (a) Sessler, J. L.; Gale, P. A.; Cho, W.-S. In Anion Receptor Chemistry; Stoddart, J. F., Ed.; Royal Society of Chemistry: Cambridge, 2006. (b) Bazzicalupi, C.; Bencini, A.; Lippolis, V. Tailoring Cyclic Polyamines for Inorganic/Organic Phosphate Binding. Chem. Soc. Rev. 2010, 39, 3709. (c) Hargrove, A. E.; Nieto, S.; Zhang, T.-Z.; Sessler, J. L.; Anslyn, E. V. Artificial Receptors for the Recognition of Phosphorylated Molecules. Chem. Rev. 2011, 111, 6603. (d) Gale, P. A.; Caltagirone, C. Anion Sensing by Small Molecules and Molecular Ensembles. Chem. Soc. Rev. 2015, 44, 4212. (e) Beer, P. D.; Gale, P. A. Anion Recognition and Sensing: The State of the Art and Future Perspectives. Angew. Chem., Int. Ed. 2001, 40, 486. (f) Wiskur, S. L.; Ait-Haddou, H.; Lavigne, J. J.; Anslyn, E. V. Teaching Old Indicators New Tricks. Acc. Chem. Res. 2001, 34, 963. (g) Wu, D.; Sedgwick, A. C.; Gunnlaugsson, T.; Akkaya, E. U.; Yoon, J.; James, T. D. Fluorescent chemosensors: the past, present and future. Chem. Soc. Rev. 2017, 46, 7105.

DOI: 10.1021/jacs.8b09021
J. Am. Chem. Soc. 2019, 141, 4597−4612

(2) (a) Mason, C. F. Biology of Freshwater Pollution; Longman: New York, 1991. (b) Busschaert, N.; Caltagirone, C.; Van Rossom, W.; Gale, P. A. Applications of Supramolecular Anion Recognition. Chem. Rev. 2015, 115, 8038.

(3) (a) Sabater, P.; Zapata, F.; Caballero, A.; Fernández, J.; Ramirez de Arellano, C.; Molina, P. 2,4,5-Trimethylimidazolium Scaffold for Anion Recognition Receptors Acting Through Charge Assisted Aliphatic and Aromatic C−H Interactions. J. Org. Chem. 2016, 81, 3790. (b) Abebayehu, A.; Dutta, R.; Kim, S.-J.; Lee, J. H.; Hwang, I.; Lee, C.-H. Synthesis and Multi-Oxo Anion-Binding Properties of Oligopyrrolic Macrocycles Based on Naphthobipyrrole. Eur. J. Org. Chem. 2016, 2016, 3959. (c) Cai, J.; Hay, B. P.; Young, N. J.; Yang, X.; Sessler, J. L. A pyrrole-based triazolium-phane with NH and cationic CH donor groups as a receptor for tetrahedral oxyanions that functions in polar media. Chem. Sci. 2013, 4, 1560.

(4) (a) Zhang, J. F.; Kim, S.; Han, J. H.; Lee, S.-J.; Pradhan, T.; Cao, Q. Y.; Lee, S. J.; Kang, C.; Kim, J. S. Pyrophosphate-Selective Fluorescent Chemosensor Based on 1,8-Naphthalimide-DPA-Zn(II) Complex and Its Application for Cell Imaging. Org. Lett. 2011, 13, 5294. (b) Kim, S. K.; Lee, D. H.; Hong, J.; Yoon, J. Chemosensors for Pyrophosphate. Acc. Chem. Res. 2009, 42, 23. (c) Lee, S.; Yuen, K. K. Y.; Jolliffe, K. A.; Yoon, J. Fluorescent and colorimetric chemosensors for pyrophosphate. Chem. Soc. Rev. 2015, 44, 1749. (d) Yu, W.-X.; Qiang, J.; Yin, J.; Kambam, S.; Wang, F.; Wang, Y.; Chen, X. Q. Ammonium-Bearing Dinuclear Copper(II) Complex: A Highly Selective and Sensitive Colorimetric Probe for Pyrophosphate. Org. Lett. 2014, 16, 2220. (e) Czarnik, A. W. Chemical Communication in Water Using Fluorescent Chemosensors. Acc. Chem. Res. 1994, 27, 302. (f) Kim, S. K.; Singh, N. J.; Kwon, J.; Hwang, I. C.; Park, S. J.; Kim, K. S.; Yoon, J. Fluorescent Imidazolium Receptors for the Recognition of Pyrophosphate. Tetrahedron 2006, 62, 6065. (g) Singh, N. J.; Jun, E. J.; Chellappan, K.; Thangadurai, D.; Chandran, R. P.; Hwang, I. C.; Yoon, J.; Kim, K. S. Quinoxaline Imidazolium Receptors for Unique Sensing of Pyrophosphate and Acetate by Charge Transfer. Org. Lett. 2007, 9, 485. (h) Jung, J. Y.; Jun, E. J.; Kwon, Y.-U.; Yoon, J. Recognition of myo-Inositol 1,4,5-Trisphosphate Using a Fluorescent Imidazolium Receptor. Chem. Commun. 2012, 48, 7928. (i) Deliomeroglu, M. K.; Lynch, V. M.; Sessler, J. L. Non-cyclic formylated dipyrromethanes as phosphate anion receptors. Chem. Sci. 2016, 7, 3843. (j) Sessler, J. L.; Cai, J.; Gong, H.-Y.; Yang, X.; Arambula, J. F.; Hay, B. P. A Pyrrolyl-Based Triazolophane: A Macrocyclic Receptor With CH and NH Donor Groups That Exhibits a Preference for Pyrophosphate Anions. J. Am. Chem. Soc. 2010, 132, 14058.

(5) (a) Cao, Q. Y.; Pradhan, T.; Kim, S.; Kim, J. S. Ferrocene-Appended Aryl Triazole for Electrochemical Recognition of Phosphate Ions. Org. Lett. 2011, 13, 4386. (b) Hirsch, A. K. H.; Fischer, F. R.; Diederich, F. Phosphate Recognition in Structural Biology. Angew. Chem. Int. Ed. 2007, 46, 338. (c) Yoon, J.; Kim, S. K.; Singh, N. J.; Lee, J. W.; Yang, Y. J.; Chellappan, K.; Kim, K. S. Highly Effective Fluorescent Sensor for $H_2PO_4^-$. J. Org. Chem. 2004, 69, 581. (d) Plitt, P.; Gross, D. E.; Lynch, V. M.; Sessler, J. L. Dipyrrolyl-Functionalized Bipyridine-Based Anion Receptors for Emission-Based Selective Detection of Dihydrogen Phosphate. Chem.- Eur. J. 2007, 13, 1374. (e) Chowdhury, B.; Sinha, S.; Ghosh, P. Selective Sensing of Phosphates by a New Bis-heteroleptic Ru^{II} Complex through Halogen Bonding: A Superior Sensor over Its Hydrogen-Bonding Analogue. Chem.- Eur. J. 2016, 22, 18051.

(6) (a) Suzuki, I.; Ui, M.; Yamauchi, A. Supramolecular Probe for Bicarbonate Exhibiting Anomalous Pyrene Fluorescence in Aqueous Media. J. Am. Chem. Soc. 2006, 128, 4498. (b) Rodríguez-Vázquez, N.; Amorín, M.; Alfonso, I.; Granja, J. R. Anion Recognition and Induced Self-Assembly of an α,γ-Cyclic Peptide To Form Spherical Clusters. Angew. Chem. Int. Ed. 2016, 55, 4504. (c) Kado, S.; Otani, H.; Nakahara, Y.; Kimura, K. Highly selective recognition of acetate and bicarbonate by thiourea-functionalised inverse crown ether in aqueous solution. Chem. Commun. 2013, 49, 886.

(7) (a) Reyheller, C.; Kubik, S. Selective Sensing of Sulfate in Aqueous Solution Using a Fluorescent Bis(Cyclopeptide). Org. Lett. 2007, 9, 5271. (b) Schaly, A.; Belda, R.; García-España, E.; Kubik, S. Selective Recognition of Sulfate Anions by a Cyclopeptide-Derived Receptor in Aqueous Phosphate Buffer. Org. Lett. 2013, 15, 6238. (c) Kubik, S.; Kirchner, R.; Nolting, D.; Seidel, J. A Molecular Oyster: A Neutral Anion Receptor Containing Two Cyclopeptide Subunits with a Remarkable Sulfate Affinity in Aqueous Solution. J. Am. Chem. Soc. 2002, 124, 12752. (d) Qin, L.; Hartley, A.; Turner, P.; Elmes, R. B. P.; Jolliffe, K. A. Macrocyclic squaramides as anion receptors with high sulfate binding affinity and selectivity in aqueous media. Chem. Sci. 2016, 7, 4563. (e) Fatila, E. M.; Twum, E. B.; Sengupta, A.; Pink, M.; Karty, J. A.; Raghavachari, K.; Flood, A. H. Anions Stabilize Each Other inside Macrocyclic Hosts. Angew. Chem. Int. Ed. 2016, 55, 14057. (f) Zhou, H.; Zhao, Y.; Gao, G.; Li, S.; Lan, J.; You, J. Highly Selective Fluorescent Recognition of Sulfate in Water by Two Rigid Tetrakisimidazolium Macrocycles with Peripheral Chains. J. Am. Chem. Soc. 2013, 135, 14908. (g) Sessler, J. L.; Katayev, E.; Pantos, D. G.; Scherbakov, P.; Reshetova, M. D.; Khrustalev, V. N.; Lynch, V. M.; Ustynyuk, Y. A. Fine Tuning the Anion Binding Properties of 2,6-Diamidopyridine Dipyrromethane Hybrid Macrocycles. J. Am. Chem. Soc. 2005, 127, 11442−11446. (h) Shumilova, T. A.; Ruffer, T.; Lang, H.; Kataev, E. A. Straightforward Design of Fluorescent Receptors for Sulfate: Study of Non-Covalent Interactions Contributing to Host−Guest Formation. Chem.- Eur. J. 2018, 24, 1500.

(8) (a) Duke, R. M.; Veale, E. B.; Pfeffer, F. M.; Kruger, P. E.; Gunnlaugsson, T. Colorimetric and Fluorescent Anion Sensors: An Overview of Recent Developments in the Use of 1,8-Naphthalimide-Based Chemosensors. Chem. Soc. Rev. 2010, 39, 3936. (b) Martínez-Máñez, R.; Sancenón, F. Chemodosimeters and 3D Inorganic Functionalised Hosts for the Fluoro-Chromogenic Sensing of Anions. Coord. Chem. Rev. 2006, 250, 3081. (c) Gunnlaugsson, T.; Glynn, M.; Tocci, G. M.; Kruger, P. E.; Pfeffer, F. M. Anion Recognition and Sensing in Organic and Aqueous Media Using Luminescent and Colorimetric Sensors. Coord. Chem. Rev. 2006, 250, 3094. (d) dos Santos, C. M. G.; Harte, A. J.; Quinn, S. J.; Gunnlaugsson, T. Recent Developments in the Field of Supramolecular Lanthanide Luminescent Sensors and Self-Assemblies. Coord. Chem. Rev. 2008, 252, 2512. (e) Li, A.-F.; Wang, J.-H.; Wang, F.; Jiang, Y.-B. Anion Complexation and Sensing Using Modified Urea and Thiourea-Based Receptors. Chem. Soc. Rev. 2010, 39, 3729. (f) Moragues, M. E.; Martínez-Máñez, R.; Sancenón, F. Chromogenic and Fluorogenic Chemosensors and Reagents for Anions. A Comprehensive Review of the Year 2009. Chem. Soc. Rev. 2011, 40, 2593. (g) Santos-Figueroa, L. E.; Moragues, M. E.; Climent, E.; Agostini, A.; Martínez-Máñez, R.; Sancenón, F. Chromogenic and Fluorogenic Chemosensors and Reagents for Anions. A Comprehensive Review of the Years 2010−2011. Chem. Soc. Rev. 2013, 42, 3489. (h) Martínez-Máñez, R.; Sancenón, F. Fluorogenic and Chromogenic Chemosensors and Reagents for Anions. Chem. Rev. 2003, 103, 4419. (i) Beer, P. D.; Gale, P. A.; Chen, G. Z. Mechanisms of Electrochemical Recognition of Cations, Anions and Neutral Guest Species by Redox-Active Receptor Molecules. Coord. Chem. Rev. 1999, 185−186, 3−36. (j) Evans, N. H.; Beer, P. D. A Ferrocene Functionalized Rotaxane Host System Capable of the Electrochemical Recognition of Chloride. Org. Biomol. Chem. 2011, 9, 92. (k) Evans, N. H.; Serpell, C. J.; Beer, P. D. A Redox-Active [3]Rotaxane Capable of Binding and Electrochemically Sensing Chloride and Sulfate Anions. Chem. Commun. 2011, 47, 8775. (l) Sun, X.; Dahlhauser, S. D.; Anslyn, E. V. New Autoinductive Cascade for the Optical Sensing of Fluoride: Application in the Detection of Phosphoryl Fluoride Nerve Agents. J. Am. Chem. Soc. 2017, 139, 4635.

(9) (a) Aucejo, R.; Diaz, P.; García-España, E.; Alarcon, J.; Delgado Pinar, E.; Torres, F.; Soriano, C.; Guillem, M. C. Naphthalene Containing Polyamines Supported in Nanosized Boehmite Particles. New J. Chem. 2007, 31, 44. (b) Miao, R.; Zheng, Q. Y.; Chen, C. F.; Huang, Z. T. A Novel Calix[4]arene Fluorescent Receptor for Selective Recognition of Acetate Anion. Tetrahedron Lett. 2005, 46, 2155. (c) Mittapalli, R. R.; Namashivaya, S. S. R.; Oshchepkov, A. S.; Kuczyńska, E.; Kataev, E. A. Design of anion-selective PET probes based on azacryptands: the effect of pH

DOI: 10.1021/jacs.8b09021
J. Am. Chem. Soc. 2019, 141, 4597−4612

on binding and fluorescence properties. Chem. Commun. 2017, 53, 4822.
(10) (a) Nishizawa, S.; Kato, Y.; Teramae, N. Fluorescence Sensing of Anions via Intramolecular Excimer Formation in a Pyrophosphate-Induced Self-Assembly of a Pyrene-Functionalized Guanidinium Receptor. J. Am. Chem. Soc. 1999, 121, 9463. (b) Birks, J. B.; Christophorou, L. G. Excimer Formation in Polycyclic Hydrocarbons and their Derivatives. Nature 1963, 197, 1064. (c) Valeur, B. Molecular Fluorescence: Principles and Applications; Wiley-VCH: Weinheim, 2001. (d) Yu, C.; Yam, V. W.-W. Glucose sensing via polyanion formation and induced pyrene excimer emission. Chem. Commun. 2009, 1347.
(11) (a) Kurishita, Y.; Kohira, T.; Ojida, A.; Hamachi, I. Rational Design of Fret-Based Ratiometric Chemosensors for in vitro and in Cell Fluorescence Analyses of Nucleoside Polyphosphates. J. Am. Chem. Soc. 2010, 132, 13290. (b) Puthiyedath, T.; Bahulayan, D. A click-generated triazole-tethered oxazolone-pyrimidinone dyad: A highly selective colorimetric and ratiometric FRET based fluorescent probe for sensing azide ions. Sens. Actuators, B 2017, 239, 1076. (c) Ren, C.; Wang, H.; Mao, D.; Zhang, X.; Fengzhao, Q.; Shi, Y.; Ding, D.; Kong, D.; Wang, L.; Yang, Z. When Molecular Probes Meet Self-Assembly: An Enhanced Quenching Effect. Angew. Int. Ed. 2015, 54, 4823.
(12) Xu, Z.; Xiao, Y.; Qian, X.; Cui, J.; Cui, D. Ratiometric and Selective Fluorescent Sensor for Cu^{II} Based on Internal Charge Transfer (ICT). Org. Lett. 2005, 7, 889.
(13) (a) Zhang, X.; Guo, L.; Wu, F.-Y.; Jiang, Y.-B. Development of Fluorescent Sensing of Anions under Excited-State Intermolecular Proton Transfer Signaling Mechanism. Org. Lett. 2003, 5, 2667. (b) Wu, Y.; Peng, X.; Fan, J.; Gao, S.; Tian, M.; Zhao, J.; Sun, S. Fluorescence Sensing of Anions Based on Inhibition of Excited-State Intramolecular Proton Transfer. J. Org. Chem. 2007, 72, 62.
(14) (a) Hu, R.; Leung, N. L. C.; Tang, B. Z. AIE macromolecules: syntheses, structures and functionalities. Chem. Soc. Rev. 2014, 43, 4494. (b) Li, X.; Ma, K.; Zhu, S.; Yao, S.; Liu, Z.; Xu, B.; Yang, B.; Tian, W. Fluorescent Aptasensor Based on Aggregation-Induced Emission Probe and Graphene Oxide. Anal. Chem. 2014, 86, 298. (c) Baglan, M.; Atılgan, S. Selective and sensitive turn-on fluorescent sensing of arsenite based on cysteine fused tetraphenylethene with AIE characteristics in aqueous media. Chem. Commun. 2013, 49, 5325. (d) Gao, C.; Gao, G.; Lan, J.; You, J. An AIE active monoimidazolium skeleton: high selectivity and fluorescence turn-on for $H_2PO_4^-$ in acetonitrile and ClO_4^- in water. Chem. Commun. 2014, 50, 5623. (e) Chen, L.-J.; Ren, Y.-Y.; Wu, N.-W.; Sun, B.; Ma, J.-Q.; Zhang, L.; Tan, H.; Liu, M.; Li, X.; Yang, H.-B. Hierarchical Self-Assembly of Discrete Organoplatinum(II) Metallacycles with Polysaccharide via Electrostatic Interactions and Their Application for Heparin Detection. J. Am. Chem. Soc. 2015, 137, 11725. (f) Watt, M. M.; Engle, J. M.; Fairley, K. C.; Robitshek, T. E.; Haley, M. M.; Johnson, D. W. Off-on" aggregation-based fluorescent sensor for the detection of chloride in water. Org. Biomol. Chem. 2015, 13, 4266.
(15) (a) Cai, J.; Sessler, J. L. Neutral CH and cationic CH donor groups as anion receptors. Chem. Soc. Rev. 2014, 43, 6198. (b) Gale, P. A.; Howe, E. N. W.; Wu, X.; Spooner, M. J. Anion receptor chemistry: Highlights from 2017. Coord. Chem. Rev. 2018, 375, 333. (c) Gale, P. A.; Howe, E. N. W.; Wu, X. Anion Receptor Chemistry. Chem. 2016, 1, 351.
(16) (a) Renney, C. M.; Fukuhara, G.; Inoue, Y.; Davis, A. P. Binding or aggregation? Hazards of interpretation in studies of molecular recognition by porphyrins in water. Chem. Commun. 2015, 51, 9551. (b) Shen, J.-S.; Li, D.-H.; Ruan, Y.-B.; Xu, S.-Y.; Yu, T.; Zhang, H.-W.; Jiang, Y.-B. Supramolecular aggregation/ disaggregation-based molecular sensing: a review focused on investigations from China. Luminescence 2012, 27, 317. (c) Wang, B.; Yu, C. Fluorescence Turn-On Detection of a Protein through the Reduced Aggregation of a Perylene Probe. Angew. Chem. Int. Ed. 2010, 49, 1485. (d) Zhai, D.; Xu, W.; Zhang, L.; Chang, Y.-T. The role of "disaggregation" in optical probe development. Chem. Soc. Rev. 2014, 43, 2402. (e) Wu, J.; Zou, R.; Wang, Q.; Xue, Y.; Wei, P.; Yang, S.; Wu, J.; Tian, H. A peptide probe for the detection of neurokinin-1 receptor by disaggregation enhanced fluorescence and magnetic resonance signals. Sci. Rep. 2015, 4, 6487.
(17) Chapin, B. M.; Metola, P.; Vankayala, S. L.; Woodcock, H. L.; Mooibroek, T. J.; Lynch, V. M.; Larkin, J. D.; Anslyn, E. V. Disaggregation is a Mechanism for Emission Turn-On of ortho-Aminomethylphenylboronic Acid-Based Saccharide Sensors. J. Am. Chem. Soc. 2017, 139, 5568.
(18) Sessler, J. L.; Davis, J. M.; Kral, V.; Kimbrough, T.; Lynch, V. Water soluble sapphyrins: potential fluorescent phosphate anion sensors. Org. Biomol. Chem. 2003, 1, 4113.
(19) Gong, H.-Y.; Zhang, X.-H.; Wang, D.-X.; Ma, H.-W.; Zheng, Q.-Y.; Wang, M.-X. Methylazacalixpyridines: Remarkable Bridging Nitrogen-Tuned Conformations and Cavities with Unique Recognition Properties. Chem. - Eur. J. 2006, 12, 9262.
(20) Zhang, E.-X.; Wang, D.-X.; Zheng, Q.-Y.; Wang, M.-X. Synthesis of Large Macrocyclic Azacalix[n]pyridines (n) 5) and Their Complexation with Fullerenes C_{60} and C_{70}. Org. Lett. 2008, 10, 2565.
(21) Liu, H.-X.; He, X.; Zhao, L. Metallamacrocycle-modified gold nanoparticles: a new pathway for surface functionalization. Chem. Commun. 2014, 50, 971.
(22) Zhao, H. X.; Liu, L. Q.; Liu, Z. D.; Wang, Y.; Zhao, X. J.; Huang, C. Z. Highly selective detection of phosphate in very complicated matrixes with an off−on fluorescent probe of europium-adjusted carbon dots. Chem. Commun. 2011, 47, 2604.
(23) Parker, C. A.; Rees, W. T. Correction of Fluorescence Spectra and Measurement of Fluorescence Quantum Efficiency. Analyst 1960, 85, 587.
(24) Park, J. S.; Le Derf, F. L.; Bejger, C. M.; Lynch, V. M.; Sessler, J. L.; Nielsen, K. A.; Johnsen, C.; Jeppesen, J. O. Positive Homotropic Allosteric Receptors for Neutral Guests: Annulated Tetrathiafulvalene−Calix[4]pyrroles as Colorimetric Chemosensors for Nitroaromatic Explosives. Chem. - Eur. J. 2010, 16, 848.
(25) (a) Mulugeta, E.; He, Q.; Sareen, D.; Hong, S.-J.; Oh, J. H.; Lynch, V. M.; Sessler, J. L.; Kim, S. K.; Lee, C.-H. Recognition, Sensing, and Trapping of Bicarbonate Anions with a Dicationic meso-Bis(benzimidazolium) Calix[4]pyrrole. Chem. 2017, 3, 1008. (b) Gunnlaugsson, T.; Kruger, P. E.; Jensen, P.; Pfeffer, F. M.; Hussey, G. M. Simple naphthalimide based anion sensors: deprotonation induced colour changes and fixation. Tetrahedron Lett. 2003, 44, 8909. (c) Maton, C.; Van Hecke, K.; Stevens, C. V. Peralkylated imidazolium carbonate ionic liquids: synthesis using dimethylcarbonate, reactivity and structure. New J. Chem. 2015, 39, 461.

DOI: 10.1021/jacs.8b09021
J. Am. Chem. Soc. 2019, 141, 4597−4612